

IMPERIAL

Design and Optimisation of a Powder Feed System for In-Space Additive Manufacturing



Author:	Jack Crane
Academic Supervisor:	Dr Ajit Panesar
Second Marker:	Dr Demetrios Venetsanos
Department:	Department of Aeronautics
Course:	MEng Aeronautics with Spacecraft Engineering
Academic Year:	2024/2025
Date:	June 20, 2025

A Thesis submitted in fulfillment of requirements for the degree of
Master of Engineering in Aeronautics with Spacecraft Engineering

Abstract

Currently, demonstrations of in-space additive manufacturing are restricted to wire-fed processes. While effective, this constraint limits the versatility of in-space fabrication and, therefore, its potential to support space missions. A major barrier to broader adoption of powder-based methods in space is the challenge of storing and delivering powder in the absence of gravity. This thesis builds on previous investigations into cold spray additive manufacturing (CSAM) to design, test, and evaluate a gravity-independent powder feed system suitable for in-space applications.

A fluidised powder-bed architecture was selected, featuring a pneumatically actuated, gas-permeable piston to compact and push the powder toward an outlet. Drawing inspiration from analogous systems in aerospace propulsion, the design was developed through iterative prototyping and tested under terrestrial conditions. Key challenges addressed included powder jamming the piston as well as an insufficient force on the piston preventing it from effectively compacting the powder at the outlet. These issues were addressed through the use of a flexible dual-cone TPU piston capable of adapting to internal tank imperfections. The system was experimentally tested at inlet pressures between 2.7 and 3.5 bar, yielding mass flow rates between 20 and 60 grams per second, significantly higher than comparable systems.

The system exhibited a reasonably consistent and controllable response to varying inlet pressures, suggesting that the architecture is scalable and responsive to upstream conditions. However, efforts to numerically simulate the design under microgravity conditions were only partially successful due to time and software limitations. While no definitive evidence was found that the system performs equivalently in microgravity, preliminary simulation results suggested continued fluidisation was likely.

Although the design requires further refinement and testing, particularly in reduced-gravity environments, this work demonstrates that a fluidised, piston-driven feed system holds promise for enabling powder-based additive manufacturing beyond Earth. The findings contribute to a growing body of knowledge in gravity-independent powder handling.

Acknowledgments

First and foremost, I would like to thank Dr Ajit Panesar for allowing me to support with testing of the original COSMOS project and then taking on my self-proposed project. His advice and support on the project were invaluable.

Second, I would like to thank the technicians at the Advanced Hackspace for training me on the lathe and advising me on o-ring groove sizing.

Finally, I would also like to thank the aeronautics technicians at Imperial as they provided insight into the most effective and safe way to set up my experiments.

Contents

1	Introduction and Context	1
1.1	In-Space Manufacturing	1
1.2	Previous Work	1
1.3	Motivation	1
1.4	Aims and Objectives	2
1.5	Structure of the Report	2
2	Academic Background	3
2.1	Cold Spray	3
2.2	Fluidised Powder Bed Phenomenon	4
2.3	Fluidised Powder Feed System Design Evolution	4
2.4	Propellant Management Devices	6
2.5	Management of Bulk Powder	6
2.6	Modelling Two-Phase flow	7
3	Methodology	8
3.1	Modelling Previous Design	8
3.2	Choosing A New Feed System Architecture	9
3.3	Hopper Tank Design	10
3.4	Hopper Tank Analysis	11
3.5	Piston Design	12
3.6	Expected Behaviour	13
3.7	Experimental Setup	14
3.7.1	Layout	14
3.7.2	Data Acquisition and System Actuation	14
3.7.3	Cyclone Separator and Measurement Method	16
3.7.4	Powder	17
3.7.5	Procedure to Characterise Pressure Source	18
3.7.6	Procedure to Characterise Full System	18
3.8	Numerical Setup	19
3.8.1	Numerical Setup to Characterise Pressure Source	19
3.8.2	Numerical Setup to Characterise Full System	20
4	Results and Discussion	23
4.1	Analysis of Previous Design	23
4.2	Analysis and Testing Tank Design	24
4.3	First Test	26
4.4	Characterising Pressure Source	27

4.4.1	Initial Test	27
4.4.2	Further Investigation	27
4.4.3	Simulation	28
4.4.4	Stagnation Pressure Values	29
4.5	Mass Flow Rate Experiment	30
4.5.1	Results from an Inlet Pressure of 4 bar	30
4.5.2	Results from an Inlet Pressure of 5 bar	31
4.5.3	Results from an Inlet Pressure of 6 bar	32
4.5.4	Mass Flow Rate Analysis and Discussion	33
4.5.5	System Controllability	34
4.5.6	System Behaviour	35
4.6	Numerical Analysis of Mass Flow Rate	35
4.6.1	Results of System Under Microgravity	35
4.6.2	Results of System Under Earth's Gravity	37
5	Conclusion and Future Work	39
5.1	Research Objectives and Key Findings	39
5.2	Suggested Next Steps	40
A	Analysis of Feed Architectures	45
B	Unprocessed Simulation Images	47
C	End Cap Engineering Drawings	49
D	Mass Flow Analysis Code	51

List of Figures

2.1	Deformation and Bonding [39]	3
2.2	Test Samples of CSAM [8]	3
2.3	Different Phases of Fluidisation [12]	4
2.4	Examples of Gas and Motor Actuated Pistons from Literature	5
2.5	Example of Fluidisation at the Inlet from Literature [16]	5
2.6	Outlet Fluidised and Inlet Fluidised Designs [35]	6
2.7	Tank Vanes [10]	6
2.8	Piston Tank Diagram [35]	6
2.9	Common Powder Structures [1]	7
3.1	Previous Design	8
3.2	Simplified Geometry	8
3.3	Mesh Used	8
3.4	5 Common Powder Feed System Architectures	9
3.5	Components of the Hopper Tank	10
3.6	Solidworks Meshes Used to Analyse Tank Design	11
3.7	Piston Design Iterations	12
3.8	Diagram of Expected Behaviour	13
3.9	Setup used During Experimentation	15
3.10	Sensor Placement in Experimental Setup	15
3.11	Testing Dashboard	16
3.12	Separator Design and Implementation	17
3.13	System Diagram of Closed System	18
3.14	Starting Sand Distribution in Tank	19
3.15	Geometry of Simulation to Characterise Pressure Source	20
3.16	Geometry and Mesh Used in Numerical Investigation of Tank	21
3.17	Mesh Deformation Throughout Simulation	22
4.1	Phase Density of Old Design after 2 Seconds	23
4.2	Change of Mass in the Tank Over Time	23
4.3	Initial Powder Configuration	23
4.4	Stress Concentrations Around Tank Bolt Holes	25
4.5	Hydrostatic Pressure Testing of Tank	25
4.6	Result of First Powder Test	26
4.7	Static Pressure Readings Before and After the Tank at Different Pressures	27
4.8	Follow-up 4 bar Tests with Different Configurations	28
4.9	Static Gauge Pressure of Empty Tank Simulation	28

4.10	Velocity Magnitude of Empty Tank Simulation	29
4.11	1st Test Using a 4 bar Inlet Pressure	30
4.12	2nd Test Using a 4 bar Inlet Pressure	30
4.13	3rd Test Using a 4 bar Inlet Pressure	30
4.14	1st Test Using a 5 bar Inlet Pressure	31
4.15	2nd Test Using a 5 bar Inlet Pressure	31
4.16	3rd Test Using a 5 bar Inlet Pressure	31
4.17	1st Test Using a 6 bar Inlet Pressure	32
4.18	2nd Test Using a 6 bar Inlet Pressure	32
4.19	3rd Test Using a 6 bar Inlet Pressure	32
4.20	Mass Flow Rate Relationship with Stagnation Pressure	34
4.21	A Snapshot of the 2nd 5 bar Inlet Test	35
4.22	Numerical Results of System Under Microgravity	36
4.23	Particle Distributions from a Piston Velocity of 30 mm/s	36
4.24	Particle Distributions from a Piston Velocity of 90 mm/s	36
4.25	Numerical Results of System Under Earth's Gravity	37
4.26	Particle Distributions from a Piston Velocity of 30 mm/s	37
4.27	Particle Distributions from a Piston Velocity of 90 mm/s	38
A.1	(a) Start	45
A.2	(b) Middle	45
A.3	(c) End	45
A.4	Comparison of Suitability of Design Paradigm Unedited	45
A.5	(a) Start	46
A.6	(b) Middle	46
A.7	(c) End	46
A.8	Comparison of Difficulty of Edits Required	46
B.1	Phase Density of Old Design after 2 Seconds	47
B.2	Results of Tank FEA	47
B.3	Static Pressure of Empty Tank Simulation	48
B.4	Velocity Magnitude of Empty Tank Simulation	48
C.1	Outlet End Cap Engineering Drawing	49
C.2	Inlet End Cap Engineering Drawing	50

List of Tables

4.1 Summary of Estimated Stagnation Pressures for Each Test	29
---	----

1 Introduction and Context

1.1 In-Space Manufacturing

In-space manufacturing (ISM) encompasses techniques for fabricating, assembling and repairing structures and components directly in orbit or on other celestial bodies. Key benefits include dramatically lower launch costs (since only raw feedstock needs to be lifted), on-demand production of replacement parts and the ability to build large structures (e.g. habitats or solar arrays) beyond the size limits of launch fairings.

1.2 Previous Work

Research into ISM dates back to the Apollo era. In 1969, the Soyuz 6 mission demonstrated that welding could be performed in vacuum, laying the groundwork for subsequent research and technology demonstrations [21]. Additive manufacturing (AM) came much later, with the first experiment aboard the ISS occurring in 2014, when a polymer Fused Filament Fabrication (FFF) printer successfully produced samples for stress testing [24]. FFF works by extruding thermoplastic wire through a heated nozzle to build parts layer by layer. More recently, in January 2024, ESA deployed a metal 3D printer employing laser-wire direct-energy deposition [7]. This involved melting stainless-steel wire onto a print bed to fabricate metallic components. Wire-based feedstock systems are currently preferred, as they simplify material storage and feedrate control in the space environment and much work still needs to be done before powder-based AM methods can be demonstrated in orbit.

1.3 Motivation

The current line of research exploring Cold Spray Additive Manufacturing (CSAM) in space started with an analysis of different AM methods and how they are influenced by properties of the space environment such as microgravity, thermal constraints and elevated exposure to radiation. Despite the requirement to bring a propellant gas to orbit with the manufacturing facility, the combination of not requiring post-processing, the flexibility of being able to spray onto unprepared metal surfaces and a high deposition rate has made CSAM an attractive candidate for further research [17].

This analysis was later followed up with COSMOS, an Imperial College London project led by Dr Ajit Panesar and funded by the UK Space Agency to demonstrate the feasibility of CSAM under vacuum conditions. The demonstration was an overall success and samples of the Ti6Al4V deposit were analysed. It was identified that the porosity of the deposit was higher than expected. This is thought to be due the mass flow rate of powder being too high, meaning the particles were not accelerated to a sufficient velocity and did not deform as

expected. In addition to the sample porosity, the design of the powder hopper was hypothesised to be unsuitable for a microgravity environment. Therefore, the objectives of this research, outlined below, are underpinned by the need to rectify both the observed high porosity and the hypothesised hopper limitations under microgravity.

1.4 Aims and Objectives

As discussed in section 2.1, the porosity of the deposit from CSAM is strongly influenced by the mass flow rate of powder dispensed. This means that any future work aimed at demonstrating the quality of deposit achievable through in-space CSAM would require a system with a high level of controllability over this parameter. Equally important to the success of ground tests is the authenticity of the conditions being emulated. To minimise the uncertainty associated with extrapolating terrestrial results to operations in orbit, each subsystem must function reliably in the space environment.

These aims will be achieved through the following objectives:

- Investigate the hypothesised issues with the current design.
- Design a new architecture to solve the previous issues.
- Experimentally investigate the controllability of mass flow rate in terrestrial conditions.
- Investigate piston geometries and their impact on the system dynamics.
- Numerically simulate the design in microgravity and terrestrial conditions.
- Compare these result to validate the extrapolation into the space environment.

1.5 Structure of the Report

This report is structured to reflect the logical progression of the research, from contextual grounding through to design, implementation, and evaluation.

It begins by introducing the broader field of in-space manufacturing and the specific challenges that motivated this project, establishing the aims and objectives that guided the work. To support the technical development, the academic background chapter explores key concepts such as cold spray technology, powder fluidisation behaviour, and relevant approaches to two-phase flow modelling.

The core of the report focuses on the methodology used to develop and assess the powder feed system—from early design considerations and hardware development to experimental procedures and simulation strategies. This is followed by a discussion of results, which brings together findings from physical testing and numerical modelling to evaluate system performance under both Earth and microgravity conditions.

Finally, the report concludes by reflecting on how well the project met its objectives and by suggesting avenues for further refinement and investigation. Supporting material, including design drawings, simulation outputs, and analysis code, is provided in the appendices to ensure transparency and reproducibility.

2 Academic Background

2.1 Cold Spray

Most engineering alloys, including stainless steel, aluminium and titanium, will undergo solid-state bonding when two atomically flat and clean surfaces are brought into contact, particularly in vacuum environments, where surface contamination is minimal [19]. This phenomenon is known as cold welding and occurs because the surface energy of the separated metal interfaces is higher than that of the bonded state, making direct bonding thermodynamically favourable [37].

Designs typically aim to prevent this for space applications, but it is the core mechanism that underpins CSAM. By accelerating metal powder particles to supersonic velocities and then impacting them onto the substrate, the particles cold weld to the surface, forming a deposit. As seen in Figure 2.1, the particles plastically deform on impact, causing the disruption and removal of the oxide layer, and exposing clean metal surfaces. The removal of the oxide layer is

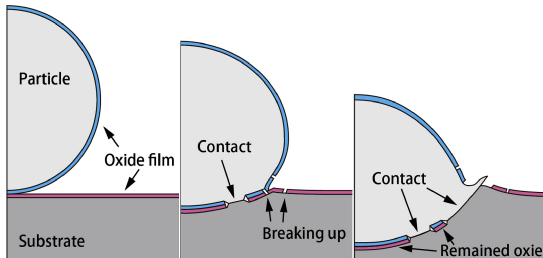


Figure 2.1: Deformation and Bonding [39]

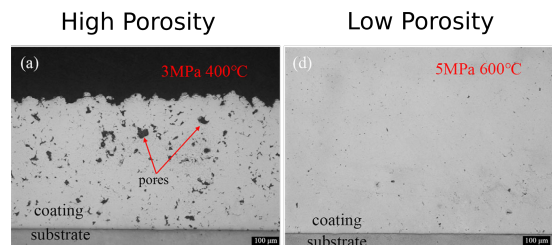


Figure 2.2: Test Samples of CSAM [8]

thought to result from adiabatic shear instability at the particle-substrate interface [2]; however, the precise mechanisms remain a topic of ongoing research and debate within the field [11].

A unique advantage of CSAM is that it is a solid-state manufacturing process. Because the material never transitions through a liquid phase, thermal input remains low, preserving the original microstructure of both the powder and the underlying substrate. This minimises issues such as residual thermal stresses, material oxidation and chemical composition inhomogeneity [25]. While solid-state manufacturing also tends to be better at reducing porosity, Figure 2.2 shows that this can still be a problem depending on the parameters of the system.

Arguably the most important parameter is the velocity of the particle impacting the surface. If this velocity is too low then bonding does not occur and if it is too high the powder roughens or erodes the substrate [9]. This velocity is dependent on the choice, pressure and temperature of accelerant gas and properties of the powder such as mass flow rate, size, shape and hardness. All of these must be carefully chosen or controlled to produce high-quality deposits.

2.2 Fluidised Powder Bed Phenomenon

Given that fluidisation underlies the design architecture presented later, the physics behind a generic fluidised powder bed are outlined in this section. The powder in these systems exhibits distinctive fluid-mechanical behaviour once a sufficient gas flow is passed upward through the granular solid [13]. As shown in Figure 2.2, as the gas velocity increases from zero, the powder initially remains fixed, with the gas passing through void spaces, known as a fixed bed regime. At a critical threshold, the minimum fluidisation velocity, the drag force exerted by the gas equals the effective weight of the particles, causing the bed to loosen and particles to become suspended. At this threshold, the pressure drop across the bed reaches a plateau, approximately

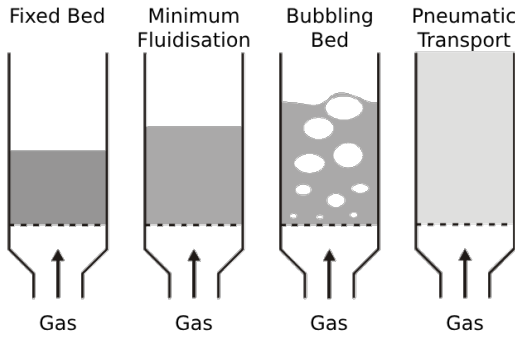


Figure 2.3: Different Phases of Fluidisation [12]

matching the weight of the solid particles per unit area. The powder itself begins to swell in volume, a phenomenon known as bed expansion. This expansion corresponds to an increase in average porosity as particles are pushed further apart in the fluid-like suspension. With further increases in gas flow, the fluidised bed exhibits bubbling behaviour. In gas-fluidised systems at ambient pressure, any gas in excess of that required to just fluidise the bed passes through in the form of buoyant gas voids or bubbles [28].

At the particle scale, motion results from the interplay of buoyancy, drag, and either cohesive or gravitational forces, depending on the particle size. For smaller particles with a diameter of $20\ \mu\text{m}$, numerical studies have shown that cohesion dominates, while particles of $75\ \mu\text{m}$ are more influenced by gravity [32]. This means that the equilibrium for heavier particles may break down in microgravity, making space-based applications particularly challenging to predict or analyse. While research exists on particle dynamics under microgravity conditions, no literature was found specifically on the behaviour of fluidised powder beds or how to model them in a low gravity environment. Therefore, the effects of microgravity on the fluidisation physics are considered out of scope for this project and have been disregarded, with the assumption that fluidisation will still occur due to cohesion.

2.3 Fluidised Powder Feed System Design Evolution

The final architecture chosen in section 3.2 draws heavily from research into metallic powder-fed engines. As both systems have strict requirements for mass flow rate control and miniaturisation, this analysis can be used to inform a more elegant design. These systems have undergone

multiple revisions to optimise performance, and this timeline is outlined to better explain the design's behaviour.

A commonly cited first implementation of a fluidising powder feed system consists of a cylindrical tank with a piston used to constrain the powder to the outlet [15]. As this paper is no longer in the public domain, exact parameters are unknown, but developments from this design can be grouped into three phases.

The first of these improvements is the use of a gas-actuated piston instead of one driven by a motor [35]. Examples of both approaches are shown in Figure 2.4. The additional mass of an electric motor, along with the electrical systems to support it, can be avoided by rerouting the high-pressure line present near the tank.

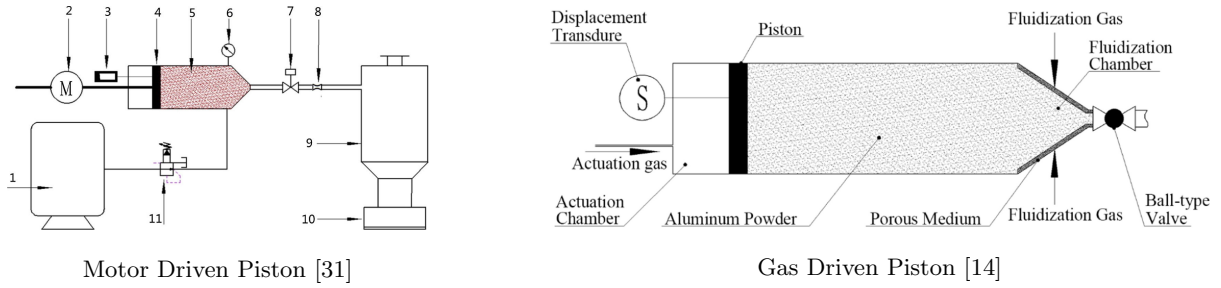


Figure 2.4: Examples of Gas and Motor Actuated Pistons from Literature

The second innovation involved fluidising the powder from both the piston face and the end of the tank, as shown in Figure 2.5. It has been demonstrated that fluidising further back in the tank results in higher mass flow rates and reduces the amount of powder left in the system [34]. This means the feed systems fluidised at the inlet have a broader operating range of mass flow rates.

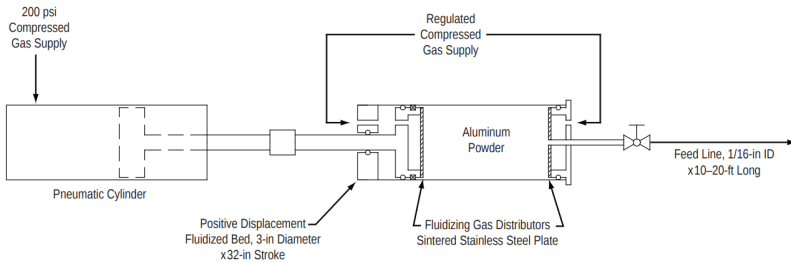


Figure 2.5: Example of Fluidisation at the Inlet from Literature [16]

The final revision was removing the fluidisation at the end of the tank entirely, as seen in Figure 2.6. Designing the tank outlet to include a porous medium in its walls requires additional structural reinforcement, which increases the overall mass. Furthermore, the extra plumbing needed to supply fluidising gas to the outlet adds unnecessary mass, which can be avoided by fluidising solely from the rear.

Powder feed systems for powder-fed rocket motors have many similarities with CSAM feed systems but differ in one notable respect. While the particles in cold spray are fed into atmospheric conditions, or vacuum conditions for space applications, the particles in an engine are fed into the high-pressure combustion chamber. This means that the downstream pressure in

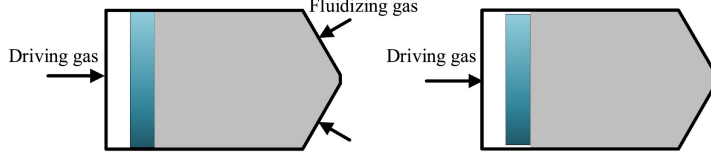


Figure 2.6: Outlet Fluidised and Inlet Fluidised Designs [35]

the two systems differ significantly, which explains why the majority of the literature focuses on high-pressure powder feed systems. Given that lower pressures, $< 1 \text{ MPa}$, are less extensively investigated, this report contributes to the analysis of such conditions.

2.4 Propellant Management Devices

The need to store material in space is not new and has received extensive research attention, particularly in the context of propellant storage. Like the manufacturing system presented later, propulsion systems can be disturbed or damaged if the contents of the tank are not properly constrained to the outlet [10]. Solutions to this problem already exist in the form of propellant management devices. Vanes, seen in Figure 2.7, sponges and galleries have been well tested in



Figure 2.7: Tank Vanes [10]

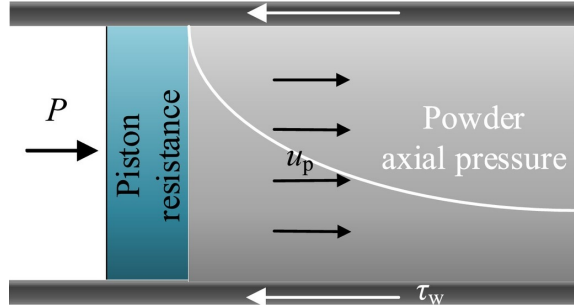


Figure 2.8: Piston Tank Diagram [35]

microgravity environments [10] but they rely on surface tension and are therefore only applicable to storing liquid. Positive expulsion devices such as bladders, diaphragms and pistons, seen in Figure 2.8, mechanically force propellant towards the outlet, and are thus suitable for powder applications.

In addition to enabling more reliable powder dispensation, constraining the powder can prevent problematic dynamics such as sloshing from occurring within the tank. This reduces the system's footprint on the rest of the spacecraft and simplifies attitude control.

2.5 Management of Bulk Powder

Powder in a tightly-packed (bulk) form exhibits entirely different dynamics from powder in a fluidised state and is more complex to describe. This complexity arises from the different types of interparticle forces [38], the changing nature of contact points and friction due to plastic and elastic deformation [33] and the limited freedom for particles to rearrange. This means powders respond to stress in a manner intermediate between a fluid and a frictional solid: they dilate

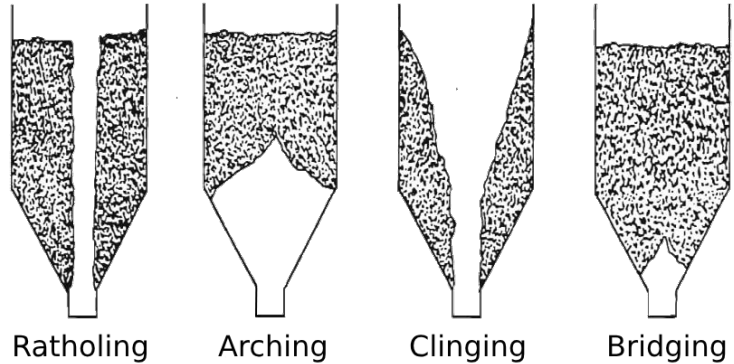


Figure 2.9: Common Powder Structures [1]

under shear, compact under normal load, and can sustain stable structures, such as those shown in Figure 2.9, that block flow in hoppers.

2.6 Modelling Two-Phase flow

Given the high cost of conducting experiments in microgravity, this project relies on correlating simulated behaviour under gravity with the experimental results, and then comparing this with the simulations conducted under microgravity conditions. Therefore, the simulation model used is outlined below.

Due to the wide variety of two-phase flow types, there are numerous ways to model the behaviour. The general idea applies the conservation of mass, momentum and energy equations for both phases over a fixed control volume. While this formulation is sufficient for performing direct numerical simulation, simplifying assumptions are often made to avoid the unrealistic computational demands [6].

Fluidising beds are typically simulated using one of two main approaches: the Eulerian-Lagrangian method or the Eulerian-Eulerian method [40]. The Eulerian-Lagrangian treats the particles as a discrete phase and the fluidising gas as a continuum. It tracks the dynamics of individual particles in a Lagrangian reference frame and couples them to the gas through interphase momentum exchange [30]. The Eulerian-Eulerian method models both phases as interpenetrating continua, tracking the local volume fraction of the particle phase and using constitutive equations from granular flow theory to couple the two [40]. As discussed in section 3.8, the Eulerian-Eulerian model is most applicable to the system under study and is therefore outlined further.

While the drag model is not a constitutive equation in the strict sense, it functions as one in Eulerian-Eulerian models by closing the system of equations. Therefore the choice of drag model significant impacts the resulting dynamics, particularly with respect to the behaviour of bubbles and bed expansion. The Gidaspow model has found to be the most representative for fluidised beds [40].

3 Methodology

3.1 Modelling Previous Design

Because microgravity is incredibly costly to achieve experimentally, a numerical investigation of the previous design was conducted using ANSYS Fluent. The transient simulation was run twice, once with gravity and once without, to compare the distribution of powder within the tank and the resulting mass flow rate.

Initially, an axisymmetric simulation using square cells of 0.4mm was attempted. This configuration was chosen because it could run as quickly as a 2D simulation, due to the reduced number of cells, while still capturing the 3D physics of the real system. It was assumed that the fine mesh allowed for strong, non-physical, flow gradients to be resolved as the simulation was numerically unstable and repeatedly crashed. To address this, a new 2D simulation with a coarser mesh of 1mm square cells was performed, shown in Figure 3.3. While the 2D nature

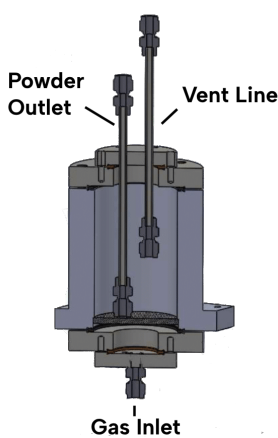


Figure 3.1: Previous Design

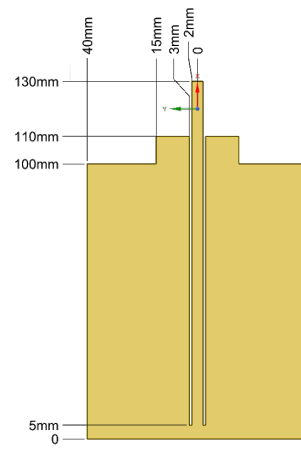


Figure 3.2: Simplified Geometry

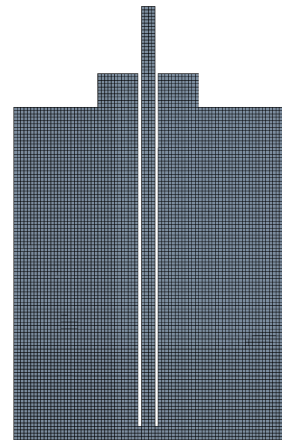


Figure 3.3: Mesh Used

of the simulation means the quantities such as mass flow rate and inlet conditions cannot be matched exactly to the real system, the key flow characteristics of interest are still expected to persist. This is because particle position within the tank and the onset of fluidisation are not strongly dependent on three-dimensional effects.

A simplified geometry, seen in Figure 3.2, was used to reduce computational time while preserving the essential geometric features. It is important to note that the vent line pipe was omitted and the outlet pipe was moved to the center; neither of these modifications were expected to affect the behaviour under investigation.

The bottom of the tank held a wire mesh on which the powder rested, representing the lower geometric boundary. In the simulation, this mesh acted as a velocity inlet, with gas entering the system at a velocity of 0.1m/s.

To simulate the two gas and powder phases, an Eulerian-Eulerian model was employed along

with the Gidaspow drag model, which has been shown to best represent fluidised beds [40]. The powder was modelled as Ti6AL4V, consistent with the material used during COSMOS. Titanium alloy powder used in selective layer sintering (SLS) has a particle size distribution between $15\ \mu\text{m}$ and $53\ \mu\text{m}$ and a density ranging from $2.04\ \text{g}/\text{cm}^3$ to $2.34\ \text{g}/\text{cm}^3$ [18], which is assumed to be similar to the powder used in CSAM. Hence a representative particle size of $40\ \mu\text{m}$ and a density of $2200\ \text{kg}/\text{m}^3$ were used.

The gas was modelled as nitrogen at standard operating conditions, consistent with its use in COSMOS.

3.2 Choosing A New Feed System Architecture

As discussed in section 4.1, the results of the analysis into the previous design supported the hypothesised issues. Consequently, a new design was deemed necessary, and a review of current powder feed technologies was conducted to better understand the strengths and limitations of prior systems. Although a thorough review of analogous systems was undertaken, it remains possible that some key papers were overlooked. The only research found on powder-based AM experiments conducted in microgravity originate from the Fraunhofer Institute; yet, this report offers limited detail on the powder-feed mechanism employed [23].

Accordingly, five common terrestrial powder-dispensing methods, shown in Figure 3.4, were examined, comparing both their suitability for use in the space environment without modifications and the complexity of implementing any necessary adaptations. Only basic schematics

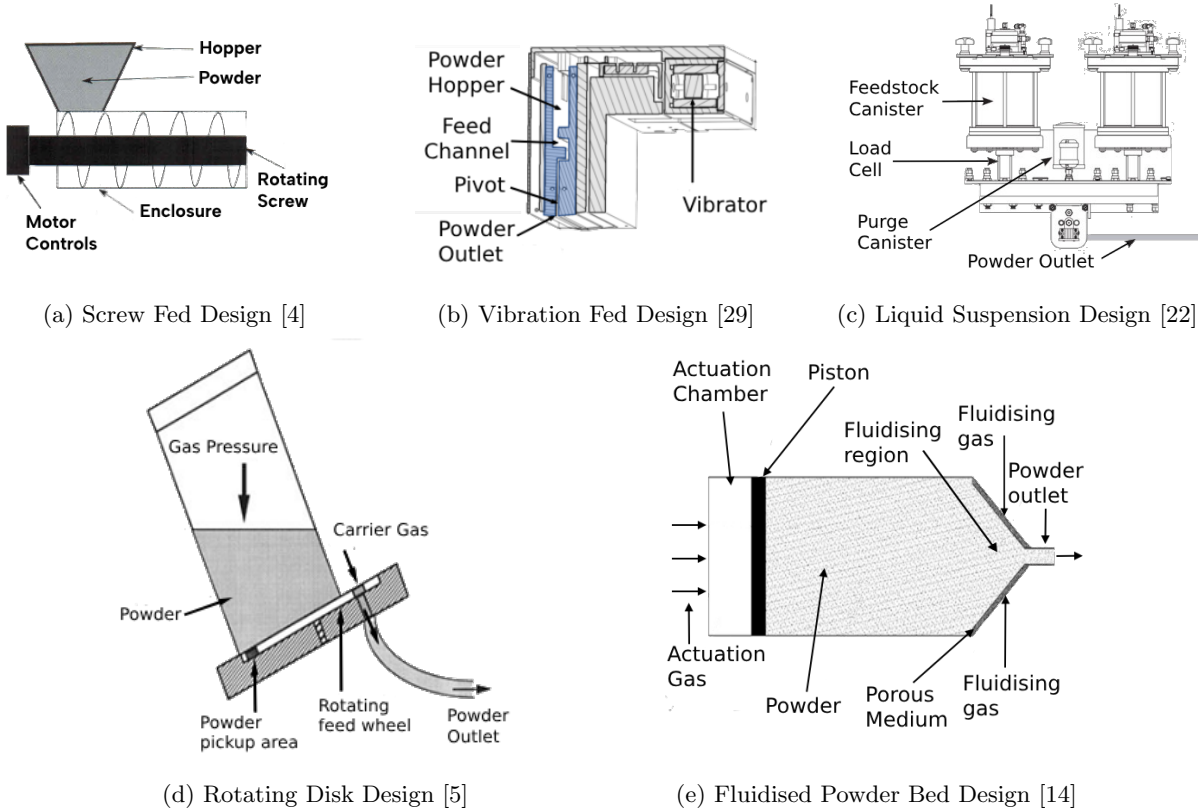


Figure 3.4: 5 Common Powder Feed System Architectures

of these methods are presented as the details of the unselected architectures are not relevant and the selected architecture is already outlined in section 2.3. The full analysis is tabulated in Appendix A. The fluidised powder bed design was selected as the most promising architecture because, like the CSAM method itself, it requires pneumatic systems, thereby mitigating this as a drawback when compared to other architectures. Furthermore, this method is assumed to be less affected by microgravity than other options, as the dominant forces acting on the particle are fluid mechanical in nature, requiring no adjustments of the core mechanic of feeding.

As discussed in section 2.3, the fluidised powder bed architecture has gone through a number of design iterations since its first implementation, primarily driven by miniaturisation requirements. To align this investigation with state-of-the-art systems, the pneumatically driven, permeable piston architecture was selected.

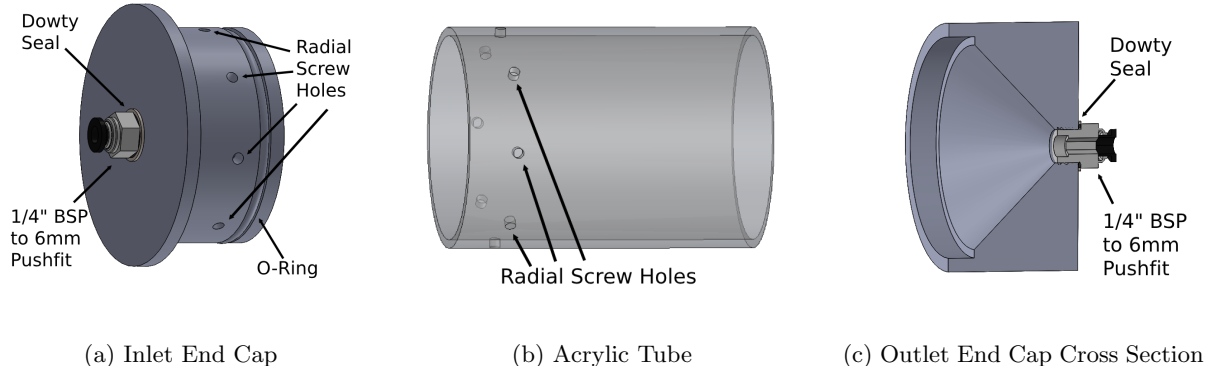
3.3 Hopper Tank Design

In fluidised powder feed systems, the tank serves a dual purpose. When not in operation, it acts as a storage vessel, securely holding the powder in a fluidisable state. During operations, the same tank functions as a delivery mechanism, enabling controlled powder dispensing through piston actuation and the introduction of fluidising gas.

Based on prior experience with the CSAM system used in COSMOS, successful samples were produced with inlet pressures between 5 and 8 bar. Therefore, 8 bar was selected as the design operating pressure for the tank. It is expected that this subsystem will experience pressure lower than or equal to the rest of the system and therefore be able to facilitate tests with an inlet pressure of 8 bar.

Although the standard safety factor for pressure vessels is 3.5 to 4 [26], this was not known at the time of design and was only discovered after manufacturing. In future iterations, this would be addressed by increasing wall thickness of the tank as well as using radial bolts to secure the outlet end cap to the tube.

The end caps were manufactured from Acetal C POM Delrin due to its low-cost, ease of machining and chemical inertness. The main tube was made from clear acrylic to allow for visual observations of flow behaviour. Upon evaluation, polycarbonate would have been a more suitable material, as it is significantly less prone to shattering [27]. As seen in Figure 3.5, the



inlet end cap is radially screwed into the tube. This design choice was made to allow the end cap to be removed for testing different piston designs. The outlet end cap was bonded to the tube using a plastic-compatible epoxy adhesive.

3.4 Hopper Tank Analysis

To validate that the design could operate up to a pressure up to 8 bar during experimentation, a combination of hand calculations and finite element analysis (FEA) using SolidWorks was performed. The failure modes analysed included stress concentrations around the bolt holes and hoop stress rupture. Fracturing at the Delrin-epoxy interface was also a concern; however, due to the lack of relevant literature on modelling this behaviour, it was not investigated further. Bolt tear-out was not analysed, as the number and length of bolts made it an unlikely failure mode.

To assess the stress distribution around the bolt holes, a static force simulation was conducted using two different mesh resolutions, as shown in Figure 3.6. The force on the bolt

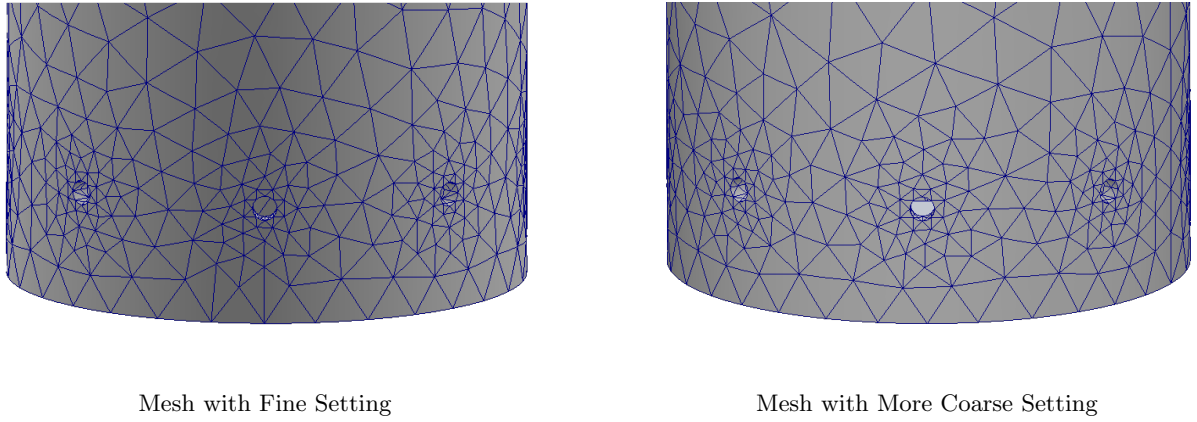


Figure 3.6: Solidworks Meshes Used to Analyse Tank Design

holes was assumed to result from the pressure acting on the end cap face due to a 7 bar pressure differential, neglecting any effect from the o-ring seal. This force was calculated using the equation:

$$F = P \cdot A.$$

$$F = 700,000 \text{ Pa} \cdot (0.037 \text{ m}^2 \cdot \pi) = 3,010 \text{ N}.$$

This force was applied to only the bottom half of each bolt hole's cross-section, representing the region where the bolt makes contact with the surface. The acrylic was modelled using SolidWorks' predefined medium-high impact acrylic, with a Young's modulus of 3 GPa and a yield stress of 45 MPa.

These material properties were also used in hand calculations to investigate hoop stress rupture as a potential failure mode. The tank was treated as a thick-walled cylinder and hoop stress was calculated using Lamé's equation [20]:

$$\sigma_\theta(r) = \frac{p_i r_i^2 - p_o r_o^2}{r_o^2 - r_i^2} + \frac{(p_o - p_i) r_i^2 r_o^2}{(r_o^2 - r_i^2) r^2}.$$

where the outer radius, r_o , was 0.04m and the inner radius, r_i , was 0.037m. The external pressure, p_o , was taken as atmospheric (approximately 1 bar) and the internal pressure, p_i , was modelled as 8 bar.

3.5 Piston Design

The primary function of the piston in this design is to constrain the powder at the outlet of the device. By modelling the powder as a fluid, the force required by the piston to pack the sand against the outlet can be calculated through the hydrostatic pressure equation:

$$P = \rho * h * g.$$

The pressure differential across the piston generated by the fluidising gas flow must counteract both this pressure from the powder and the frictional force between the piston and the tank walls to ensure effective compaction. However, due to the non-linear nature of granular material's affect on friction, modelling this interaction in detail was deemed beyond the scope of the project. Additionally, manufacturing imperfections in both the tank tube and piston prevented accurate modelling of the flow field around the piston, making the expected pressure differential across it too complex to simulate reliably. Although the piston design holds significant potential for system optimisation, time constraints of the project limited further investigation.

Given these complexities, the initial piston geometry, seen in Figure 3.7 (a), was modelled after a previous study, which found that a gear-like geometry offered the best performance in a gas-permeable powder feed system [35]. The first piston was designed under the assumption

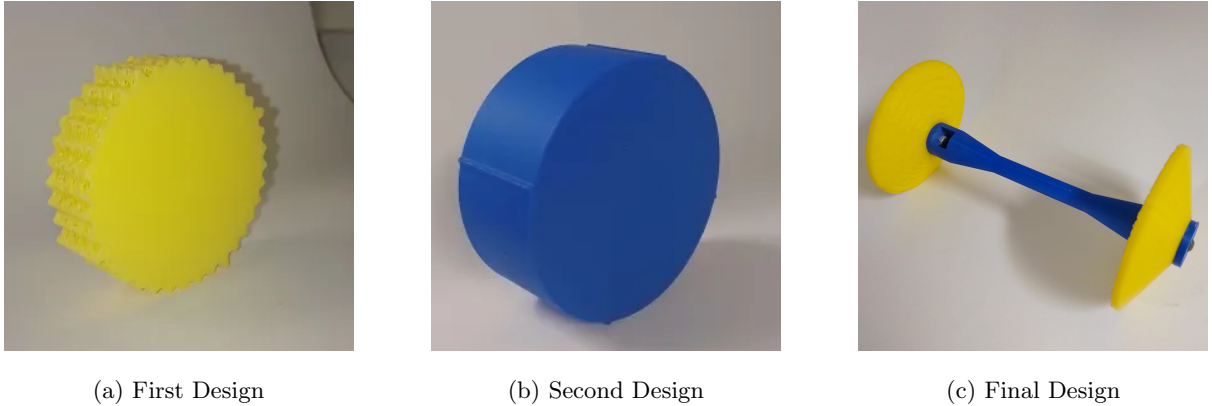


Figure 3.7: Piston Design Iterations

that the high pressure within the tank would not equalise quickly enough with the pressure inside the printed piston, causing it to crumple or deform. To address this, the wall layers were omitted during 3D printing to allow for pressure equalisation. However preliminary testing revealed that this design did not generate sufficient pressure force to move down the tank, prompting a second iteration.

Building on this insight, the second piston was designed to constrict the flow around its perimeter as much as possible to increase the pressure differential acting on it. As discussed in section 4.3, this piston was able to move under pressure but became immediately jammed by

the sand, motivating the third redesign focused on preventing jamming.

The final piston consists of 2 3D-printed TPU cones, each 3mm thick, connected by a 100mm PLA rod. The flexibility of TPU provided critical resilience against jamming, allowing individual grains to be flexed around so that the piston could continue compacting the remaining sand. In addition to the material change, increasing the piston's length helped mitigate jamming due to axis misalignment.

The dual-plate and rod configuration not only resulted in a lighter design compared to a fully TPU piston, but also reduced the contact area, lowering the risk of frictional sticking or sand-induced jamming. Moreover, the compliant nature of TPU enabled the piston face to conform to the tank's internal surface, compensating for manufacturing imperfections such as slight variations in diameter or cylindricity. This allowed for a more effective seal, enabling higher pressure differentials and more consistent compaction of the sand at the outlet.

3.6 Expected Behaviour

To predict the behaviour of the system, parallels were drawn from research looking at fluidising powder feed systems for metal powder engines. It has been proposed that the flow behaviour within the tank can be divided into two distinct regions: a dense phase moving area preceding the cone, and a fluidising region afterwards [34]. This conceptual model is interpreted in the behaviour illustrated in Figure 3.8. This analysis assumes arching occurs at the cone-tube

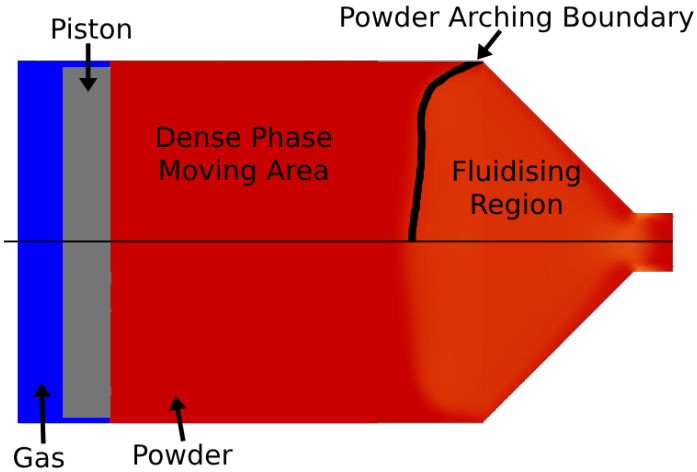


Figure 3.8: Diagram of Expected Behaviour

interface, previously discussed in section 2.5, due to both geometric constriction and pressure applied by the piston. These conditions promote the formation of a stable arching structure that constrains powder flow. The model is further supported by two findings from literature. First, the piston velocity exhibits a linear relationship with the mass flow rate dispensed from the system [31]. Second, increasing the force on the piston initially raises the mass flow rate, but beyond a certain point this effect saturates, and further increases in piston force no longer lead to higher flow rates [15].

Consider a scenario in which the piston provides minimal force on the powder. The fluidising region would then expand passed the cone-tube interface (leftwards on the diagram), similar to

bed expansion. Applying greater piston force then would compress this region down, meaning a fluidising region with a higher density of powder. This would raise the number of particles close to the outlet and available for entrainment, resulting in a higher mass flow rate. If the piston force were increased further still, the fluidising region would compress down into the cone and the dense phase moving area would reach the cone-tube interface. At this point, arching would occur and any additional force from the piston would be transferred through the powder column into the cone structure rather than compressing the fluidised region. This matches the behaviour reported in the literature, where increased piston pressure no longer increases the mass flow rate.

This interpretation places significant design constraints on the piston, which controls both the force exerted on the powder and the flow rate of fluidising gas. Both these are functions of the inlet pressure, and their coupling is non-trivial. While this interdependence complicates control, it also offers considerable advantages in terms of system miniaturisation, a trade-off considered acceptable within the scope of this design.

A second effect is also expected: a change in behaviour based on the amount of powder remaining in the tank. As discussed in section 2.2, the pressure drop across a fluidised bed approximately equals the weight of the particles per unit area in the fluidised regime. Therefore, as the total powder mass decreases, so does the effective pressure drop, implying a dynamic relationship between powder quantity and the pressure experienced by the fluidising region.

3.7 Experimental Setup

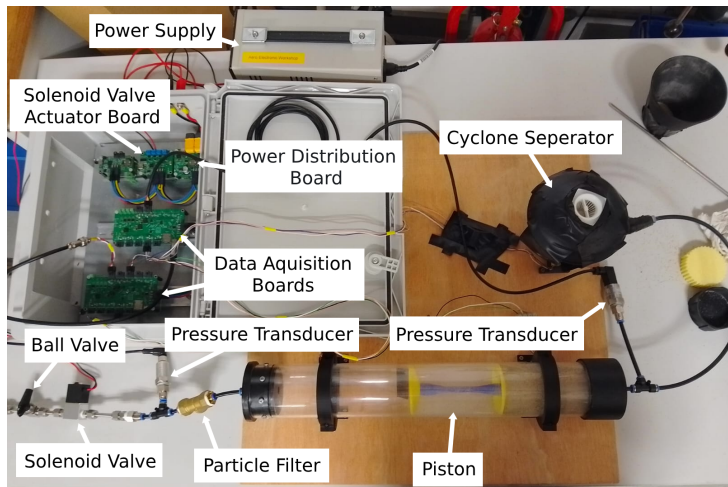
The experimental set up was designed to verify the expected behaviour of the fluidising powder feed system under terrestrial conditions to better estimate its behaviour under microgravity. The core aims were to record the consistency of the powder mass flow rate, verify that changing the pressure upstream of the tank leads to a change in mass flow rate and document any behaviours the system may exhibit that would impact its suitability for space applications.

3.7.1 Layout

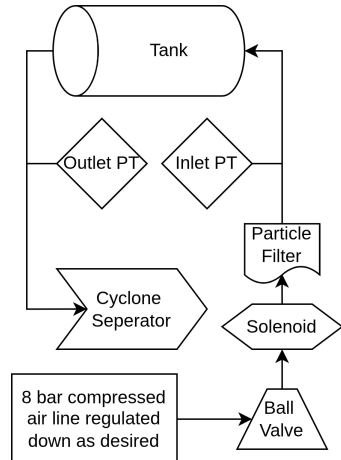
The default layout, seen in Figure 3.9, was used to perform most of the testing, with modifications outlined in the sections where they occur. Testing was conducted in Imperial College's Hypersonic Laboratory, which does not have climate control. It was assumed that the system would not behave noticeably differently under the slight variations in temperature and pressure that occurred during the testing period.

3.7.2 Data Acquisition and System Actuation

To capture the system's behaviour, a combination of video recordings, load cell readings and pressure transducer readings were taken during each test. The placement of the sensors is shown in Figure 3.10 and their values were read with the use of custom electronics designed by the Imperial College London Rocketry team. The load cells were placed at the start and end of the tank as well as beneath the cyclone separator. This was done as it allows for two independent measurements of powder mass movement to allow for cross-validation and redundancy. The

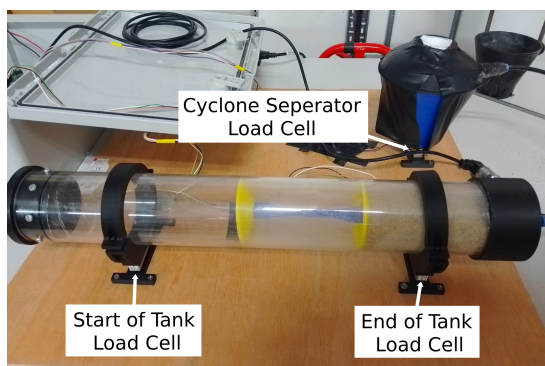


Annotated Image of Setup

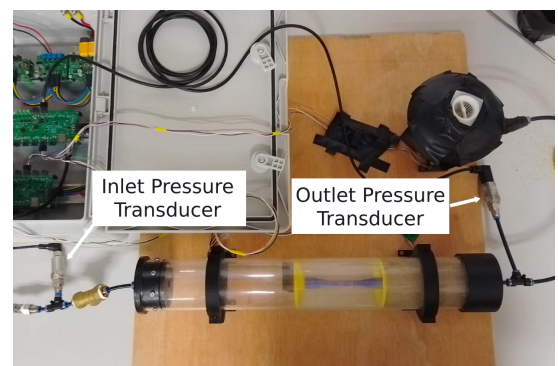


Systems Diagram of Setup

Figure 3.9: Setup used During Experimentation



Load Cell Placement



Pressure Transducer Placement

Figure 3.10: Sensor Placement in Experimental Setup

pressure transducers were placed before and after the tank with the goal of being able to use them for a deeper analysis of the system. This analysis was never conducted due to the complexity of modelling the pistons impact on the static pressure as well as time constraints of the project.

A computer was connected to the electronics system to log and display the data on a bespoke user interface, shown in Figure 3.11. The solenoid valve, seen in Figure 3.9, could also be opened and closed through the dashboard, allowing for safe operation as all the information and control was in one place. Due to budget constraints, low-cost pressure transducers and load cells were



Figure 3.11: Testing Dashboard

used. Given this, extensive calibration was not prioritised as these components typically exhibit higher variability and lower stability, limiting the benefits of precise calibration. To calibrate the load cells, the data acquisition board was configured to record the raw values output by the analog to digital converter (ADC) at both the unloaded, 0kg, state and then with a mass, measured at 0.746kg, placed on it. Since the load cells are a linear sensor, these two points give a gradient and y-intercept to map the ADC counts to. The same procedure was done to calibrate the pressure transducers except using a mechanical pressure gauge and the compressed air line to record 1 bar and 4 bar ADC outputs.

An older setup of the experiment included a choke point just after the outlet of the tank. This was because previous literature proposed that fluidising systems where one part of the gas-solid flow is in choking conditions had been found to be simpler to control [31]. Due to the grain size of the sand, this chokepoint got clogged in testing and was therefore removed. As there was a pressure transducer before and after the chokepoint, this explains the data labels in Figure 3.11 and why the pre-choke pressure data is just noise as it was no longer connected.

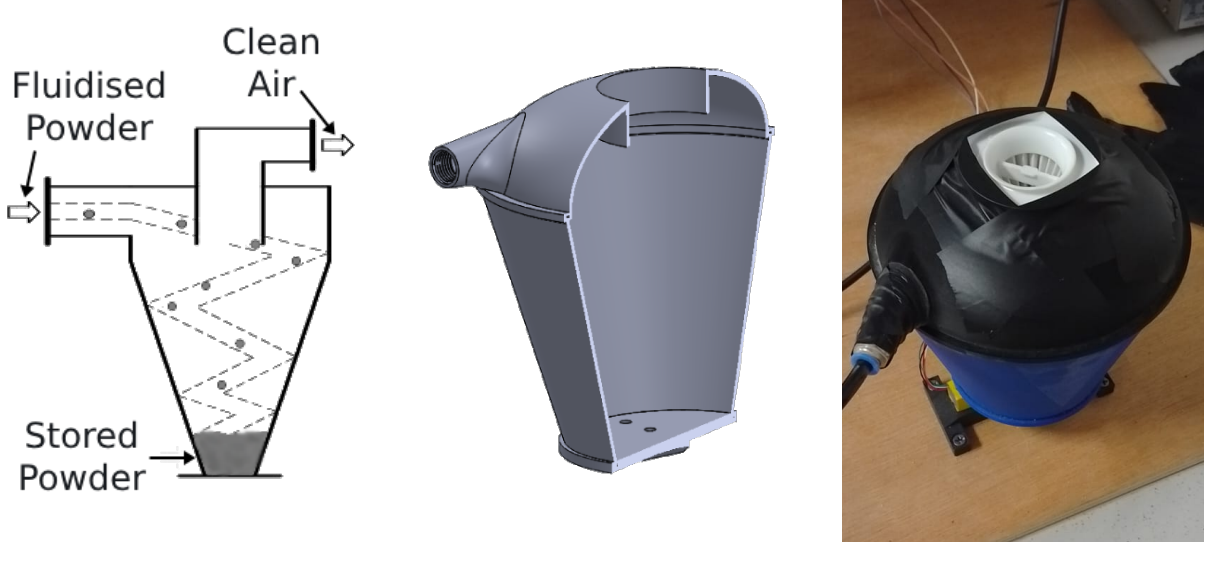
3.7.3 Cyclone Separator and Measurement Method

The two most common methods of measuring mass flow rate for this kind of system are using a displacement transducer to measure how far down the tank the piston is or measuring the mass of the powder after it has been fed out of the tank [31][15][34]. The displacement transducer method indirectly measures the mass flow by using the near incompressibility of the powder

and the assumption of a constant packing density to form a linear relationship between the movement of the piston and the volume of powder dispensed [31]. The direct method requires some method of separating the gas and powder after it has exited the system and then measures the mass of powder over time.

The direct mass measurement method was used as it had multiple advantages over measuring piston displacement. The first being there was no additional modifications to the tank end cap needed since incorporating a displacement transducer would mean a hole would have to be drilled and could provide another place for leaks to occur. If any powder found its way behind the piston it could interfere with the displacement readings and there is a risk that the piston velocity would not be constant, a concern that was validated during testing. Finally, the powder needed to be contained no matter what method was chosen as airbourne sand particles are a hazard to lung health. Therefore adding a load cell to this containment method was much easier to implement.

To contain the powder and separate out the gas, a cyclone separator was used, seen in Figure 3.12. A cyclone separator works by using centrifugal force to separate the sand from



(a) Cyclone Separator Diagram (b) CAD Model of Separator (c) Cyclone Separator

Figure 3.12: Seperator Design and Implementation

the air. As the mixture enters the cyclone chamber tangentially at high speed, it spins rapidly, causing the denser particles to move outward and fall to the bottom, while the cleaner air exits through the top center. As shown in Figure 3.12 (c), a dust filter used in vacuum cleaners was used to ensure any fine grains, not captured by the separator, did not make it out into the air. This was attached to the 3D printed model using PTFE tape and a friction fit, then taped down for added support. The separator was printed in 3 parts, the top that could be removed to empty out the sand, the walls and the base with screw holes to mount to the load cell.

3.7.4 Powder

While typical powders used in CSAM are $5\text{ }\mu\text{m}$ to $100\text{ }\mu\text{m}$ [36], budget constraints resulted in sand being the optimal granular material safe enough to work with. This will definitely affect

the behaviour of the system but to what extent is unknown. A rudimentary attempt was made to measure the particle diameter using a micrometer but given the time limitations, no formal attempt was made to characterise the diameter distributions or average diameter. As mentioned in section 3.8, the bulk density, that being the density of the sand including the volume occupied by air, was measured by recording the mass of the sand in a bowl and then filling the same bowl with water.

3.7.5 Procedure to Characterise Pressure Source

Due to safety and ease of handling, the pressurised air supplied into the system came from a compressed air line. As mentioned in section 4.3, the pressure readings from preliminary testing were lower than expected, so an attempt at characterising the air supply was made.

To do this, the steady-state flow through the system without any piston or sand was investigated by measuring the static pressure before and after the tank at different regulator settings. Tuning of the regulator was consistent across all experiments conducted and was done as follows. The system was closed by replacing the inlet pipe into the tank with a pushfit end cap, as seen in figure Figure 3.13. The regulator integrated into the compressed air line was then

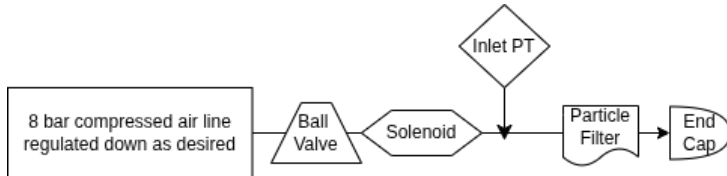


Figure 3.13: System Diagram of Closed System

adjusted using the inlet pressure transducer readings as a reference. While there was a gauge on the regulator, it was consistently reading 0.2 to 0.3 bar higher than the pressure transducers in the system or manual pressure gauges used and was therefore deemed unreliable. Once the pressure was tuned on the regulator, the valves were closed, the end cap was removed and the tube was reattached to the tank, returning to the default configuration.

Confirmation of the lower than expected static pressure readings motivated follow-up tests to eliminate possible sources of human error in the system setup. The pressure regulator integrated into the compressed air line was checked first by including another gauge closer to the system and fully opening the integrated one. If the static pressure losses were because of the 2 metres of nylon tube from the air line to the experimental setup, this would also have been highlighted.

Additionally, the solenoid valve could have had a very small orifice area, potentially choking the flow just before the pressure transducer. To test this, the valve was removed, and additional tests were conducted with the component excluded.

3.7.6 Procedure to Characterise Full System

To ensure an equal comparison between the behaviour of the system at different inlet pressure configurations, a consistent testing procedure was adhered to.

Starting from default configuration with nothing in the tank clean tank, the inlet end cap was removed and the piston was placed in it. This was positioned at the start of the tank to

lower the chance that the piston gets stuck on the sand that forms an incline, seen in Figure 3.14. If the piston had time to accelerate from far away, it was found to be more likely to sweep that



Figure 3.14: Starting Sand Distribution in Tank

ramp sand forwards with its movement and fully pack the sand into the outlet instead of getting stuck. Next the female pushfit fitting was removed from the outlet of the tank and 1000 g to 1020 g of sand was measured out and put into the tank through the use of a funnel. Once the sand had filled the tank, the pushfit fitting was reattached and a tube with an end cap was placed over the outlet. The tank was then held vertically such that the outlet was facing down and tapped to ensure no sand was stuck to the walls close to the piston, which would prevent successful startup. Then the tank was placed on the load cell stands, ensuring that the system starts with sand fully covering the cross section of the tank close to the outlet, again seen in Figure 3.14. Once placed down, the end cap tube was removed from the inlet and the tube leading to the cyclone separator was connected. The cyclone separator was then taped down to reduce the likelihood the lid pops off. It is thought that this was only necessary due to the undersizing of the cyclone separator but since taping it solved the issue, a 3rd iteration on the design was deemed unnecessary. Once the system was set up, the pressure regulator was tuned as in subsection 3.7.5. The end cap was removed from the closed system configuration and the tube was then reattached to the tank inlet.

Now that the system was ready for testing, the valves were opened and the data was logged. Ideally, the computer would have been placed far away from the system, the ball valve would have been opened and only when the solenoid valve was actuated remotely would the system function. Unfortunately, due to the solenoid valve leaking, the computer had to be placed near the system to minimise the time between opening the ball valve and actuating the solenoid. Once the pressure reading at the outlet had dropped sufficiently, it was assumed all the powder had been dispensed into the separator and the valves were closed.

3.8 Numerical Setup

3.8.1 Numerical Setup to Characterise Pressure Source

To provide an additional angle into the investigation of the pressure source behaviour, seen in section 4.4, an axisymmetric steady-state simulation was conducted of the system without a piston or powder in the tank.

The geometry used can be seen in Figure 3.15, noting the two vertices in the geometry

outlined to record the numerical values of pressure at locations similar to the pressure transducers in the experimental setup. An axisymmetric model was chosen to reduce computational



Figure 3.15: Geometry of Simulation to Characterise Pressure Source

cost by minimising the number of cells, while still capturing the essential pressure and velocity characteristics of the full 3D flow. This simplification was justified by the assumption of no angular dependence around the axis of revolution and the absence of swirl. Owing to the reduced computational time required by the axisymmetric model, a fine mesh of 0.1 mm square cells was used to enable high-resolution flow analysis. The inlet was modelled as a pressure inlet with a stagnation pressure of 2 bar, while the outlet was defined as a pressure outlet at atmospheric conditions. Air at standard operating conditions was used as the working fluid, as this is assumed to closely approximates the properties of the compressed air supply.

3.8.2 Numerical Setup to Characterise Full System

To gain more insight into how effectively the design would translate to the space environment, numerical simulations were carried out to observe key flow features. As no experimental data on fluidisation under microgravity conditions exists in the literature, options for validating the simulations were limited. Consequently, efforts were made to replicate well-documented behaviours, such as the relationship between piston velocity and mass flow rate, to establish a degree of confidence in the simulation results. In the absence of direct validation methods, these relationships served as proxies for assessing simulation validity. Due to the scope of the project, simulation methods were limited to pre-existing software, and ANSYS Fluent was selected for its capability to perform moving mesh and two-phase flow simulations with relatively low prerequisite knowledge.

Unfortunately, this numerical analysis as a whole was marred by setbacks and slow progress owing to limited educational material on how to use the more advanced aspects of Fluent and no information on where the student license differs from capabilities available for commercial license holders.

Given that the analysis aimed to replicate the linear relationship between mass flow rate and piston velocity, the most appropriate simulation to investigate this would be a 3D, two-phase, compressible flow transient simulation with a moving piston. The dimensions of the tank geometry means that 3D mesh resolutions below 1mm square cells would exceed the 1,048,576 cell limit placed on the student license, therefore this had to be altered to a 2D model. An axisymmetric model would also have been more ideal to preserve the 3D quantities of the real physics but was not possible due to gravity needing to be applied at 90 degrees to the tank's axis of revolution, creating an angular dependency on the direction of gravity the particles would

experience. Furthermore, given that the flow should be constricted and accelerated around the perimeter of the piston, flow velocities on the order of mach 0.3 are also expected meaning the incorporation of a compressible model would have been ideal but Fluent cannot run both a two-phase flow model and a compressible model, and so the flow was ran incompressibly.

Therefore, to conduct this study, a 2D, two-phase, incompressible transient flow simulation was conducted with the geometry seen in Figure 3.16 (a). The left vertex was defined as a

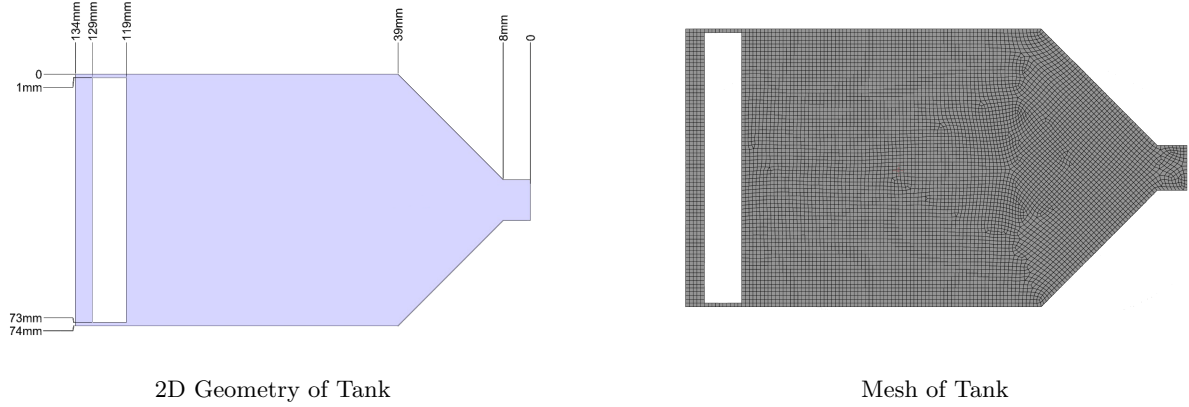
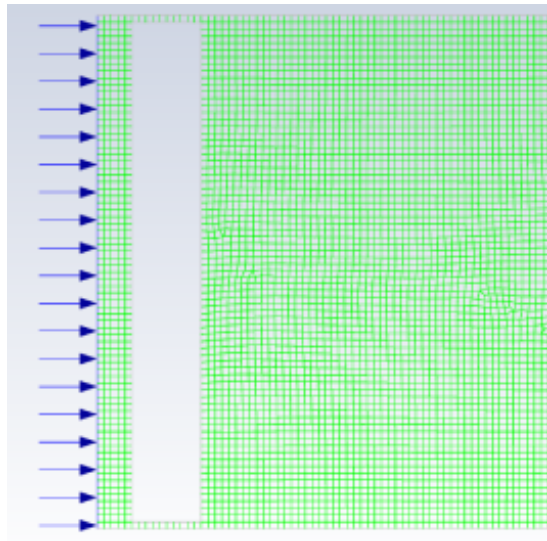


Figure 3.16: Geometry and Mesh Used in Numerical Investigation of Tank

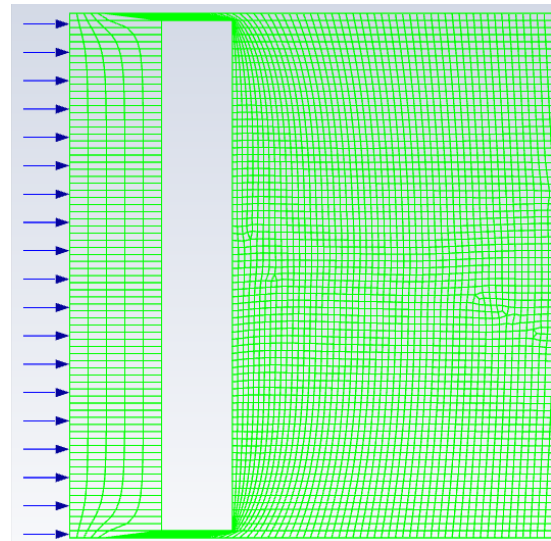
velocity inlet to avoid the backflow of powder often encountered with pressure inlet configurations. Gas entered the system at a velocity of 0.01 m/s, while both the gas and powder exited through a pressure outlet at the rightmost vertex. The white space in the geometry represented the piston, which was modelled as a moving wall. Although simulating the piston as a gas-permeable material was considered, this approach was ultimately excluded due to the added complexity it would introduce and the increased difficulty it would pose for model verification. Through iterative testing, a mesh of 1mm square cells was found to be optimal with respect to simulation stability and run time. 2000 time steps of 0.0001s were used meaning only short simulation timeframes were analysed but this still allowed for prominent flow features to be displayed.

To simulate the piston with a constant velocity, a dynamic mesh was used with smoothing and layering. Numerous attempts were made to implement remeshing to limit the skewness of cells near the piston during the simulation but none were successful. This is thought to be another limit on the student license and reduced stability of the simulation in the later half of the simulation due to deformed cells, shown in Figure 3.17. The simulations under both Earth's gravity and microgravity conditions were ran 3 times for different piston velocities. The velocities were 30mm/s, 60mm/s and 90mm/s.

The final parameters to tweak for the simulation were the two-phase flow conditions. Like section 3.1, an Eulerian-Eulerian model with a Gidaspow drag model were used as they are most appropriate for this kind of flow. To ensure that the piston accurately moved the powder down the tank, a Schaeffer frictional viscosity model and a kinetic theory of granular flow frictional pressure model adapted for dense particle conditions were used. The frictional packing limit was chosen as 0.55 but this aspect of modelling the two-phase flow was severely underinvestigated due to the time limits of the project, validated only by the videos of the simulation



(a) Mesh at Beginning of Simulation



(b) Mesh at End of Simulation

Figure 3.17: Mesh Deformation Throughout Simulation

looking reasonably close to the expected physics. Granular temperature and pressure were also investigated to better model the system but would promote numerical instability, assumably because of incorrect configuration, so were not implemented.

4 Results and Discussion

4.1 Analysis of Previous Design

To test the hypothesised issue with the previous design, animations of the 2D simulation were generated, and the change in mass of the solid phase was recorded. Figure 4.1 shows a snapshot at two seconds into the transient simulation. As illustrated, there is a marked difference in

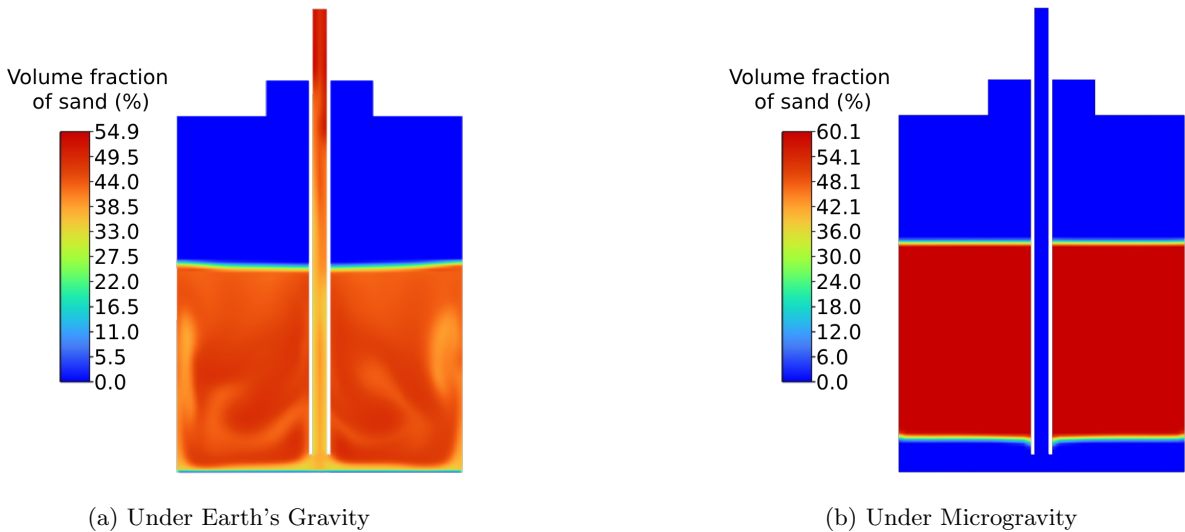


Figure 4.1: Phase Density of Old Design after 2 Seconds

the powder distribution between the two cases. While the powder in the tank under gravity appears to fully fluidise, the tank in microgravity remains relatively unaffected by the flow. This is likely because the steady-state flow field does not interact with the region of the tank where the powder settles. For completeness, all unprocessed simulation images are provided in Appendix B.

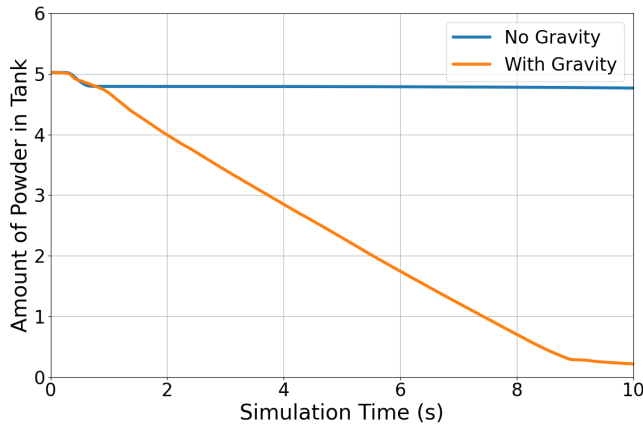


Figure 4.2: Change of Mass in the Tank Over Time

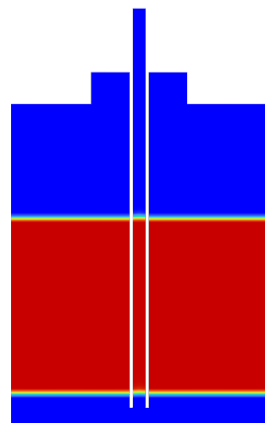


Figure 4.3: Initial Powder Configuration

Figure 4.2 presents the change in amount of powder within the tank over time, measured by integrating the volume fraction of the solid phase over the entire geometry. At roughly 0.5 seconds, both simulations exhibit a noticeable drop in powder content. This behaviour is attributed to the initial conditions of the simulation, as shown in Figure 4.3, where the powder was initially located within the pipe and was rapidly expelled from the system. Beyond this point, a significant divergence in powder dispensing rates emerges between the two cases, further supporting the hypothesis that the previous design is less suitable for microgravity applications and justifying the decision to redesign the tank.

As mentioned in section 3.1, this analysis was conducted with a relatively coarse mesh, which may have influenced the accuracy of the results. The primary concerns are the potential under-resolution of key flow gradients and inaccuracies in the momentum exchange between the two phases. However, given the simplicity of the geometry and the low inlet velocity, it is assumed that any impact from insufficient resolution of velocity or pressure gradients is minimal. The effect on momentum exchange is less certain and was considered acceptable based on the author's understanding of the expected system behavior. With additional time, this area should be explored further through a mesh convergence study to validate these preliminary findings.

Another area for improvement involves the inlet boundary condition. A pressure inlet would more accurately represent the physical system, but due to limitations in the simulation software, there was no straightforward method to prevent powder from exiting through this inlet if it were modelled that way. This issue could be addressed using a user-defined function (UDF). By first simulating the system with a pressure inlet and no powder, the resulting inlet velocity profile could be extracted and then applied to the current analysis using a UDF.

4.2 Analysis and Testing Tank Design

As mentioned in section 3.4, validation of the tank design was conducted in two stages: first through FEA and hand calculations prior to manufacturing, and then through hydrostatic pressure testing of the completed tank.

The initial FEA was performed using a configuration with six bolt holes. However, this was increased to eight after the predicted stress in the six-bolt configuration exceeded the yield strength of acrylic. As seen in Figure 4.4, the eight-bolt hole configuration shows stresses that are close to, but still below, the material's yield strength. Figure 4.4 (a) shows the original vertices of the tank under no load, overlaid in orange on the deformed tank geometry. As the difference between the undeformed and deformed shapes is minimal, nonlinear deformation effects were considered negligible. Cylindrical geometries are inherently resistant to buckling, especially when pressurised internally, so buckling was not investigated in detail.

While a slight increase in von Mises stress was observed in the finer mesh, this was attributed to improved resolution at the boundary between the loaded and unloaded surfaces of the bolt holes. Since the real load application does not exactly match the simplified simulation boundary condition, the observed stress concentrations were deemed acceptable to start manufacturing.

The next failure mode checked was hoop stress rupture, evaluated using Lamé's equations. These calculations yielded a maximum stress of 8.88 MPa at the inner wall and 8.18 MPa at

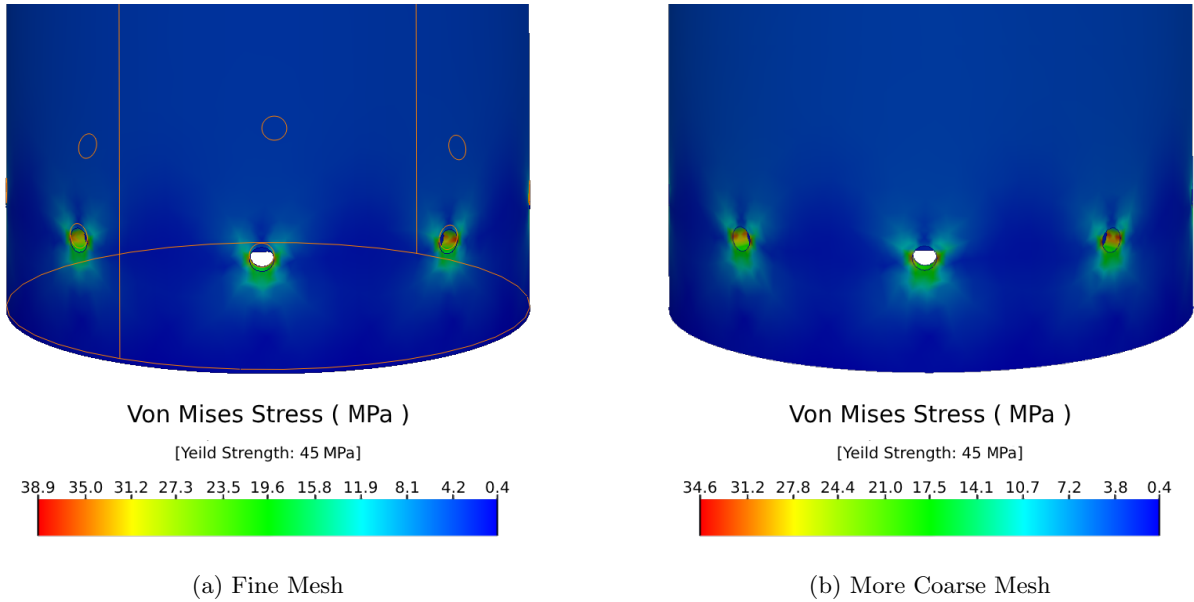


Figure 4.4: Stress Concentrations Around Tank Bolt Holes

the outer wall. As these values are significantly lower than the stress concentrations around the bolt holes, hoop stress rupture was not considered the critical failure mode.

After manufacturing, the tank underwent hydrostatic pressure testing. During the first attempt, pressurising the tank with water caused the epoxy-Delrin interface to separate. Although this failure mode was anticipated during the design phase, it was expected that reattaching the end cap using a more plastic-compatible epoxy, along with thorough surface preparation of the Delrin bonding area, would resolve the issue. This assumption was validated in the subsequent pressure test, shown in Figure 4.5. Unfortunately, only a video recording of the test was taken

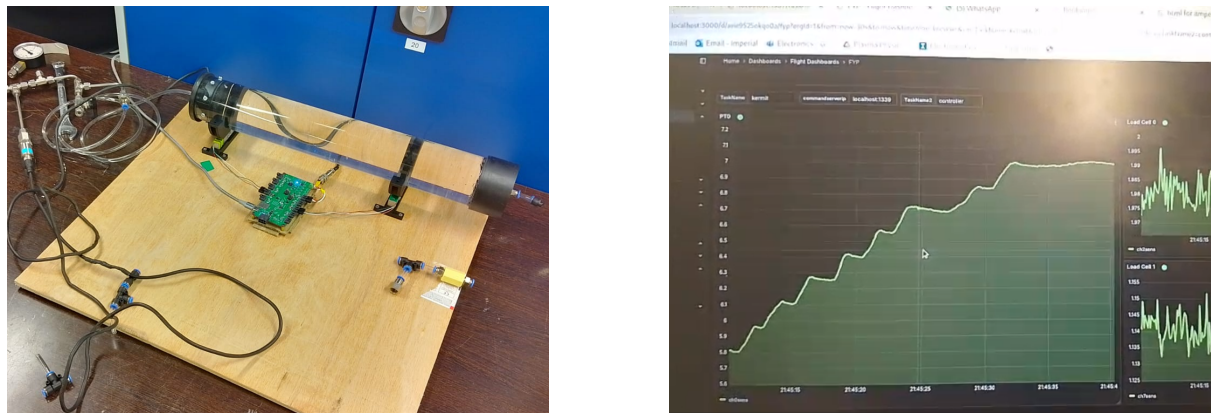


Figure 4.5: Hydrostatic Pressure Testing of Tank

and the logged pressure data was not captured. A screenshot of the video is shown in Figure 4.5 (b), where the jagged rise in gauge pressure is from the manual actuation of the pump. The tank held successfully held a gauge pressure of 7 bar for approximately 2 to 3 minutes before the pressure was released. Although maintaining pressure for a longer durations would have provided greater confidence in the tank's safety, formal pressure vessel certification was not

required for the intended experimental use and was therefore not pursued.

4.3 First Test

As mentioned in section 3.5, the initial test was conducted without sand and failed to push the piston down the tank. This quick test motivated the need to characterise the pressure source, as the pressure readings upstream and downstream of the tank were both lower and more sluggish than expected. As a result the failure mode of piston crumpling was ruled out, and subsequent piston designs did not account for this possibility. Following the characterisation of the pressure source, the second piston was tested, seen in Figure 4.6.



Figure 4.6: Result of First Powder Test

The piston initially started near the inlet of the tank and was successfully pushed toward the outlet. However, upon reaching the sand, it became stuck. The unpacked grains formed a wedge beneath the piston, causing it to jam against the tank walls. Since the powder was not compacted against the outlet, ratholing occurred, with gas entraining sand particles through the outlet—highlighting an undesirable dispensing regime.

The piston-to-wall clearance was designed to be 1 mm, the same order of magnitude as the diameter of some of the large grains of sand, so it is expected that this specific issue would not have occurred with finer-grain sand. While options such as purchasing finer sand or crushing the current sample were considered, it was ultimately decided to pursue a new design. This jamming behavior is not well reported in piston tank design literature and posed challenges for friction characterisation. Although a full analysis of the piston mechanics was of great interest, complexities in the underlying physics pushed it outside the scope of the project due to time constraints.

4.4 Characterising Pressure Source

4.4.1 Initial Test

The first step in characterising the system was to investigate the static pressure losses within the tank in the absence of a piston or any powder. This immediately revealed an issue: the static pressure readings, assuming a gas source with a stagnation pressure of 4 to 6 bar, were significantly lower than expected, as shown in Figure 4.7. If the compressed air line were truly

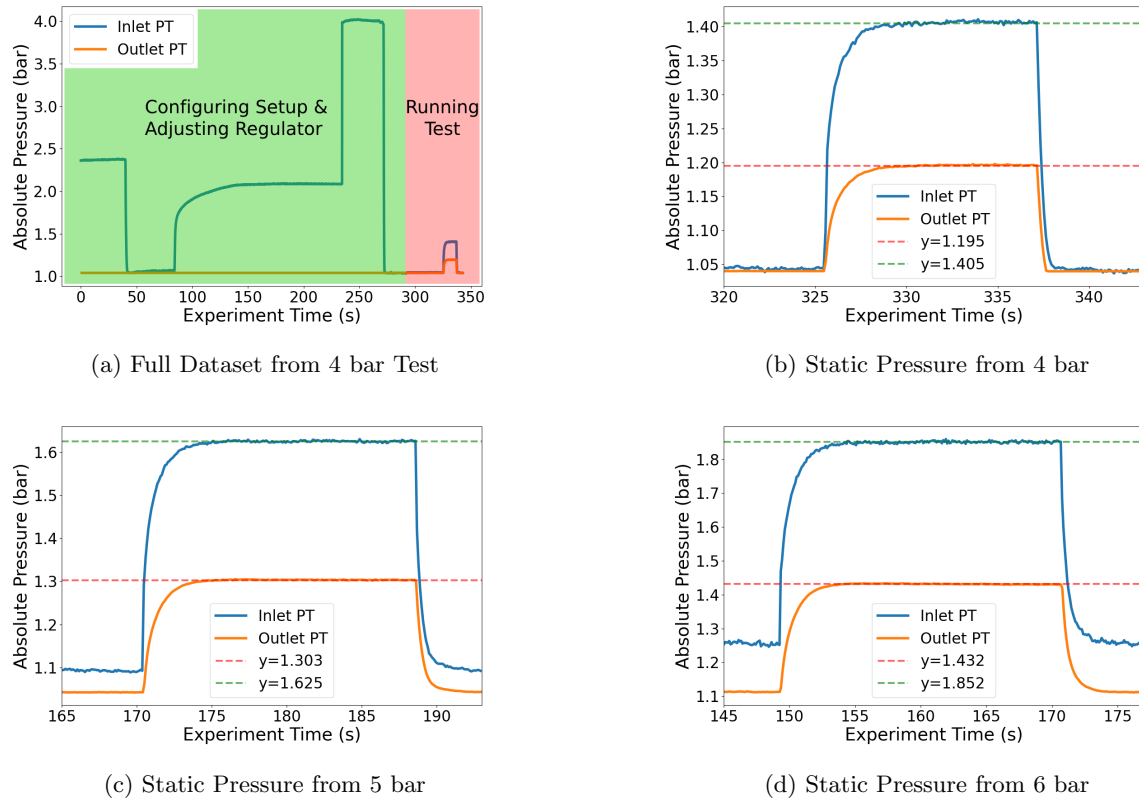


Figure 4.7: Static Pressure Readings Before and After the Tank at Different Pressures

supplying a stagnation pressure of 4 bar, isentropic flow relations suggest that the flow would have a Mach number of approximately 1.3, an unlikely result under the given conditions.

As shown in Figure 4.7 (a), the regulator was capable of maintaining a static pressure of 4 bar when the system was closed. Upon opening the system, one might expect the regulator to continue maintaining this 4 bar pressure, with only moderate reductions caused by static pressure losses and flow acceleration downstream of the regulator. However, by the time the flow reached the pressure transducer upstream of the tank, the static pressure had fallen to 1.4 bar.

4.4.2 Further Investigation

In an attempt to diagnose this behaviour, follow-up tests were conducted with different setups and a 4 bar inlet pressure to validate a component of the system was not to blame. As seen in

Figure 4.8, the performance with the additional regulator or removal of the solenoid valve was much worse giving even lower static pressure readings.

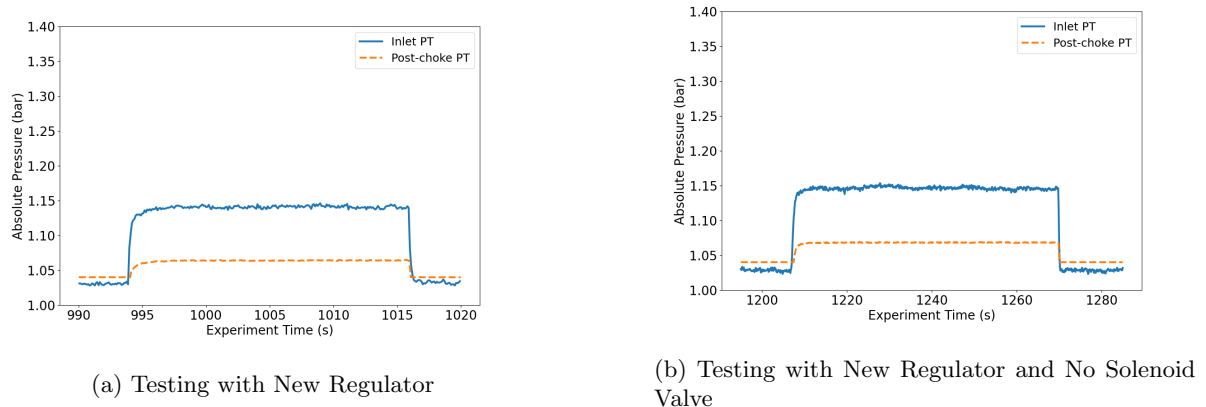


Figure 4.8: Follow-up 4 bar Tests with Different Configurations

4.4.3 Simulation

From the experimental testing, two likely explanations emerged: first, the stagnation pressure supplied to the system may have been less than 4 bar due to choking upstream of the regulator; second, the static pressure readings may have been reduced by the high velocity of the flow, resulting in elevated dynamic pressure. To further investigate the system, a 2D axisymmetric steady-state simulation of the empty tank was conducted, which appeared to support both explanations. The pressure gradient observed in the simulation, shown in Figure 4.9, yielded results comparable to the experimental pressure transducer readings, when using a gauge pressure inlet of 1 bar. The simulated pressure values at the measurement locations were 1.46 bar

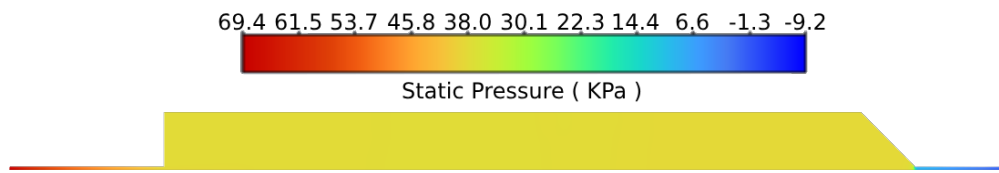


Figure 4.9: Static Gauge Pressure of Empty Tank Simulation

upstream of the tank and 1.06 bar downstream. While these are close to the experimental data, the outlet pressure was notably lower, indicating that the simulation does not fully account for the observed behaviour.

The velocity distribution from the same simulation is shown in Figure 4.10. Within just 0.1 m of pipe, the flow was found to accelerate to 275mm/s. This supports the hypothesis that a significant portion of the stagnation pressure is converted into dynamic pressure within the piping, which would explain the low static pressure readings observed experimentally.

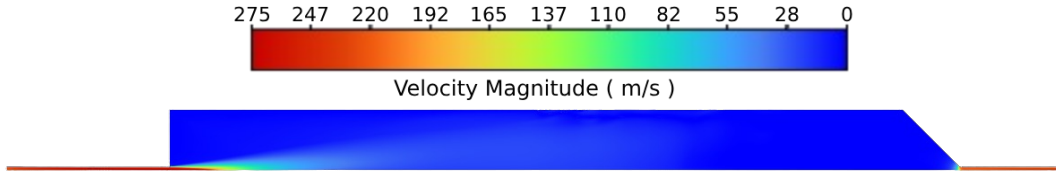


Figure 4.10: Velocity Magnitude of Empty Tank Simulation

4.4.4 Stagnation Pressure Values

Based on experimental testing, it was concluded that the observed behaviour was not the result of human error in setting up the system. Therefore, the hypothesised explanation is further supported by the numerical simulation, particularly with regard to the theorised high velocity in the pipes. As a result, to estimate the actual stagnation pressure at the inlet, isentropic relations were applied. Assuming the flow velocity reached Mach 1, the ratio of static to stagnation pressure is given by:

$$\frac{p}{p_o} = 0.52828178.$$

This relation was used to calculate the upstream stagnation pressures seen in Table 4.1 below.

	Test 1	Test 2	Test 3
Pressure Regulator Setting (bar)	4.00	5.00	6.00
Static Pressure at Inlet (bar)	1.405	1.625	1.852
Stagnation Pressure (bar)	2.66	3.08	3.51

Table 4.1: Summary of Estimated Stagnation Pressures for Each Test

4.5 Mass Flow Rate Experiment

4.5.1 Results from an Inlet Pressure of 4 bar

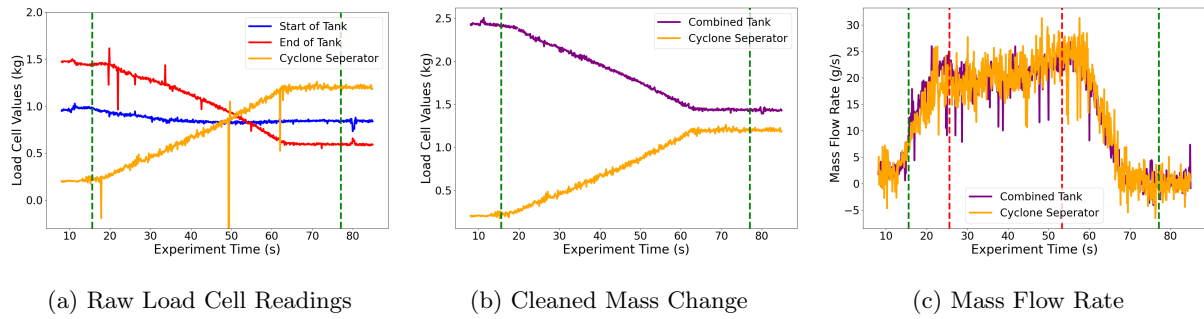


Figure 4.11: 1st Test Using a 4 bar Inlet Pressure

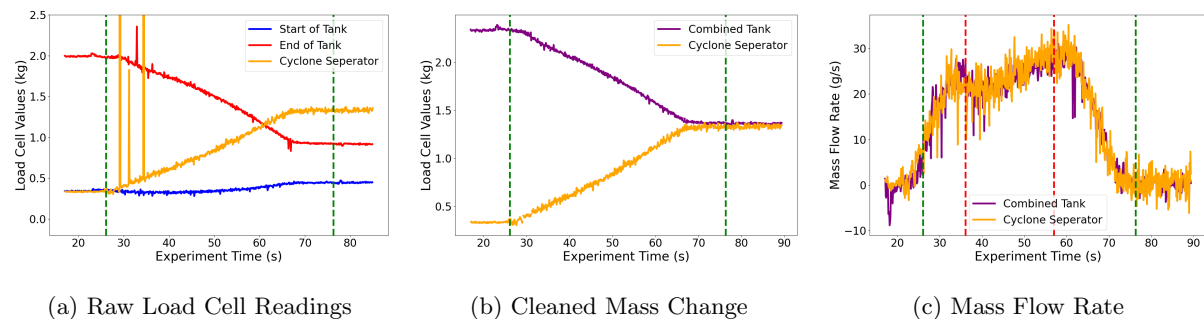


Figure 4.12: 2nd Test Using a 4 bar Inlet Pressure

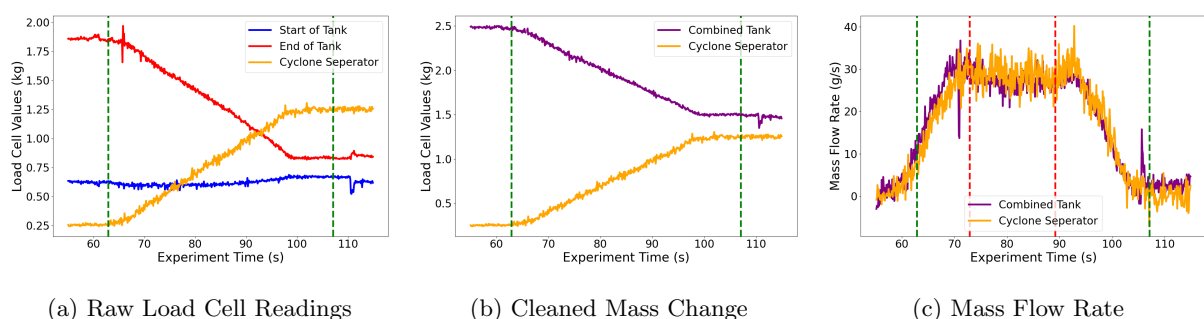


Figure 4.13: 3rd Test Using a 4 bar Inlet Pressure

4.5.2 Results from an Inlet Pressure of 5 bar

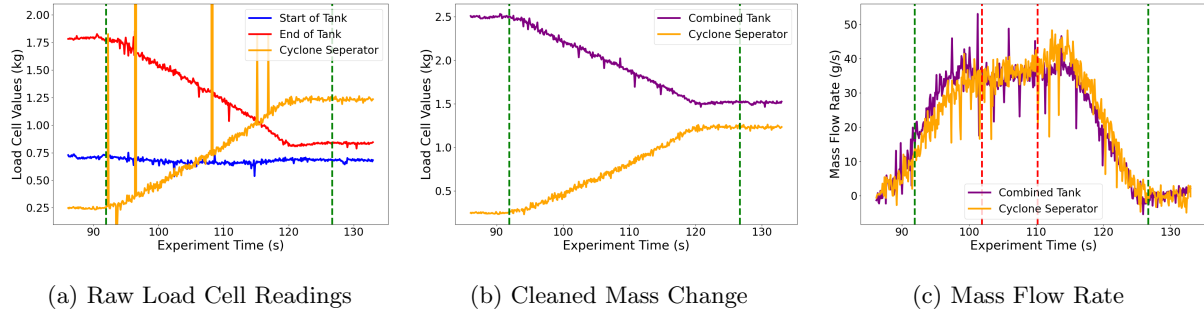


Figure 4.14: 1st Test Using a 5 bar Inlet Pressure

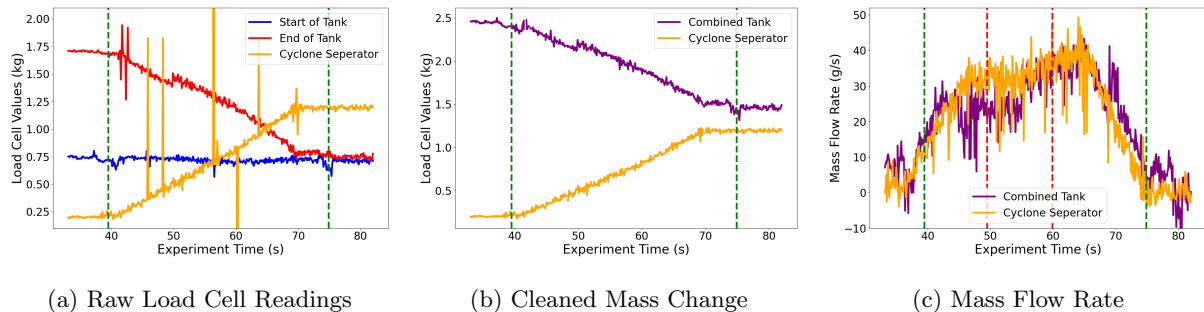


Figure 4.15: 2nd Test Using a 5 bar Inlet Pressure

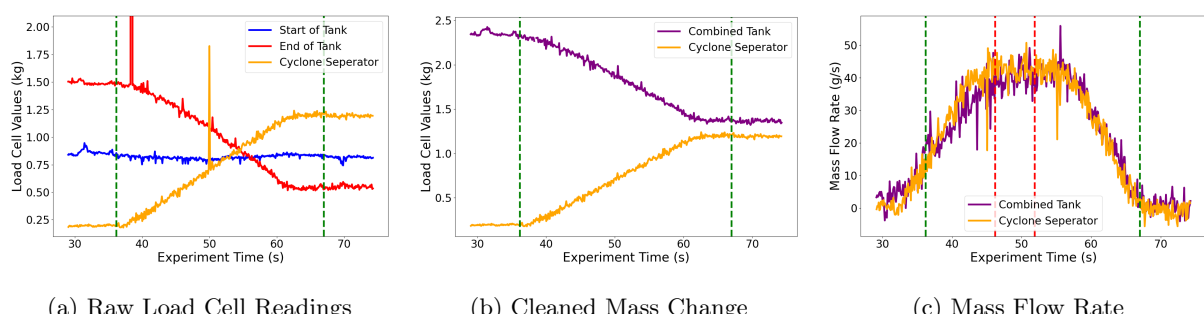


Figure 4.16: 3rd Test Using a 5 bar Inlet Pressure

4.5.3 Results from an Inlet Pressure of 6 bar

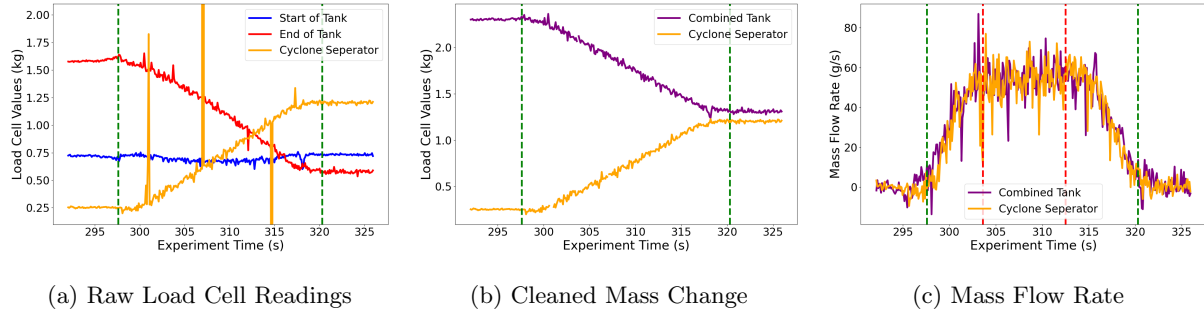


Figure 4.17: 1st Test Using a 6 bar Inlet Pressure

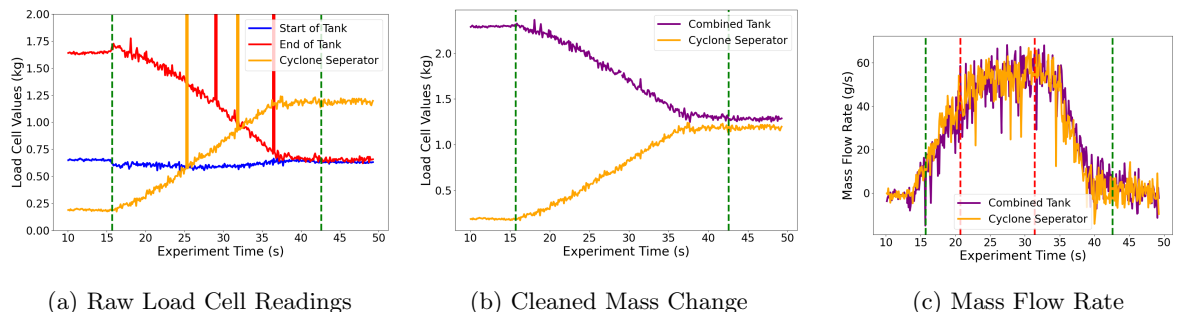


Figure 4.18: 2nd Test Using a 6 bar Inlet Pressure

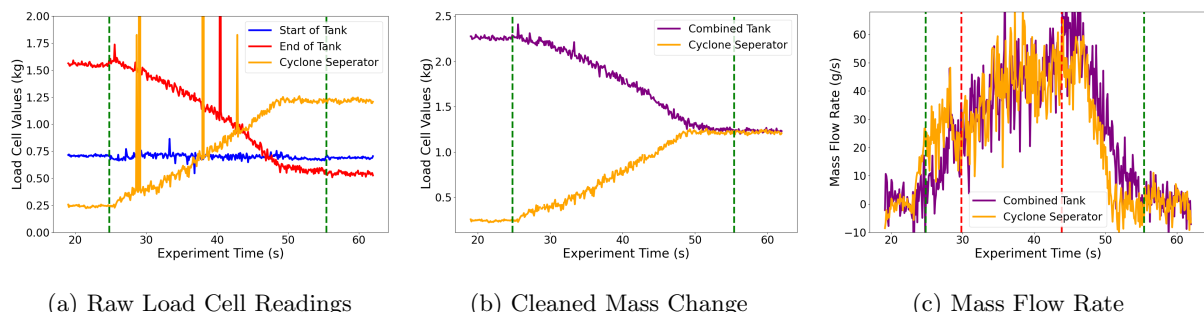


Figure 4.19: 3rd Test Using a 6 bar Inlet Pressure

4.5.4 Mass Flow Rate Analysis and Discussion

For each test, the raw load cell readings are shown in graphs (a) above. Most plots reveal the presence of noise in the readings, resulting in several data points being significantly higher or lower than the surrounding values. Although steps were taken to mitigate this, such as taping down the screw terminals in case of faulty wire connections, the issue persisted. Interestingly, the noise appears to be less common in the lower-pressure recordings, suggesting a potential link to electrostatic charge buildup in the sand due to the triboelectric effect.

Anomalous readings were manually removed, and the load cell data from the start and end of the tank were combined to compute the total mass exiting the tank over time, as shown in graphs (b) above. A simple moving average was then applied to the combined tank and cyclone separator data: a window of 100 data points was used for the 4 and 5 bar inlet pressure tests, and 50 data points for the 6 bar tests. With a sensor polling rate of 10 Hz, a 100-point moving average introduces edge distortion for up to 10 seconds after the valve is opened. Green dashed lines in the graphs indicate the valve open/close events, while red dashed lines mark the time regions considered free from edge distortion, 10 seconds after opening and 10 seconds before the mass plateau for the lower-pressure tests, and 5 seconds for the 6 bar test.

One of the most notable observations is the measured mass flow rate range of 20 g/s to 60 g/s. This is approximately three orders of magnitude greater than feed rates reported in previous systems, such as 3.5 and 5.7 g/min [3]. While this result highlights the strong scalability potential of fluidised powder feed systems, it limits the direct comparability of this system's behaviour with those described in existing literature. To address this disparity, a chokepoint could be reintroduced, provided the powder particle size is reduced to avoid clogging. However, this modification may also lower the pressure differential across the piston, potentially reducing packing efficiency.

Another key observation is the variation in mass flow rate profiles, even among tests conducted at the same inlet pressure. For instance, the three tests performed at 4 bar exhibit inconsistencies, even when analysis is limited to the region between the red dashed lines. Specifically:

- Test 1 starts around 18 g/s and ends at 25 g/s,
- Test 2 begins at 21 g/s and reaches 25 g/s,
- Test 3 remains relatively flat at 29 g/s throughout.

A gradual increase in mass flow rate over time is generally expected, as the diminishing volume of powder reduces static pressure losses associated with fluidisation. However, the behaviour observed in these tests does not follow this trend consistently. The inconsistency is likely influenced by the system's high mass flow rate and the relatively short test durations, which may mask underlying patterns or transient effects. Notably, certain tests, such as the one shown in Figure 4.5.1, exhibit remarkably stable flow rates, indicating that the variability may be due to uncharacterised factors such as local powder distribution or source pressure fluctuations. Further investigation is required to isolate these variables and better understand the root cause of the observed inconsistencies.

A final point of interest is the unexpected behaviour observed in Figure 4.15 (c), where a notable divergence appears between the mass flow rates calculated using the two measurement methods. This discrepancy is unusual, as the test was conducted under identical conditions to preceding and following tests and appeared visually consistent in the recorded footage. No obvious anomalies were identified upon review, suggesting that the cause may be related to subtle measurement errors, unobserved variations in system response, or transient disturbances not captured in the visual analysis. This highlights the need for more robust synchronisation between data acquisition methods and potentially more sensitive diagnostics to resolve such inconsistencies in future testing.

4.5.5 System Controllability

Even with the variation in mass flow rates outlined above, they still follow a general linear trend of mass flow rate increasing with static pressure, seen in Figure 4.20. While direct extrapolation

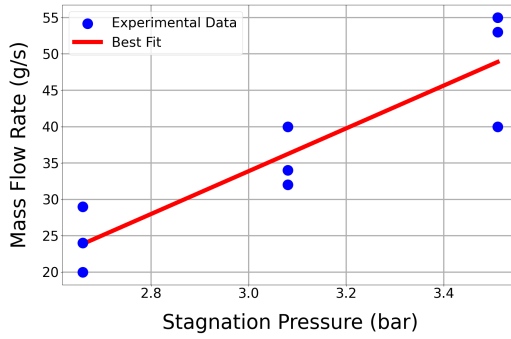


Figure 4.20: Mass Flow Rate Relationship with Stagnation Pressure

to the lower flow rates reported in the literature would be inappropriate, the results nonetheless provide strong evidence that the required inlet pressure for powder feed systems can be significantly reduced. This is a parameter that has not been thoroughly investigated in prior studies, likely because feed systems for metallic powder-fed engines are designed to inject powder into combustion chambers operating at high pressures. In such systems, reducing a relative pressure difference between the tank inlet and outlet from 10 bar to 3 bar offers limited benefits, as the combustion chamber itself may be at pressures exceeding 30 bar.

Although reducing the pressure rating of a 40 bar vessel to 33 bar yields some mass and volume savings, the impact is far more significant when reducing a 10 bar vessel to 3 bar. This makes the finding particularly valuable for ISM applications. In addition to the miniaturisation aspect, the required gas flow rate can be reduced. In space-based cold spray systems, gas is a non-renewable and limited resource. Therefore, lowering both the inlet pressure and the associated gas flow rate required for effective powder feeding provides clear advantages—specifically, reducing the quantity and pressure of gas that must be transported into space.

It should be noted, however, that the graph presented obscures an important detail: two distinct driving forces influence the mass flow rate, and these are non-trivially coupled. Therefore, further investigation into how these driving forces behave at lower pressures is required before this finding can be confidently used to inform design decisions.

4.5.6 System Behaviour

The system behaviour differed significantly from the expectations outlined in section 3.6. As seen in Figure 4.21, a fluidising region was observed in direct contact with the piston head, an unexpected result. The end cap obstructs the view of the conical section, so it remains unclear

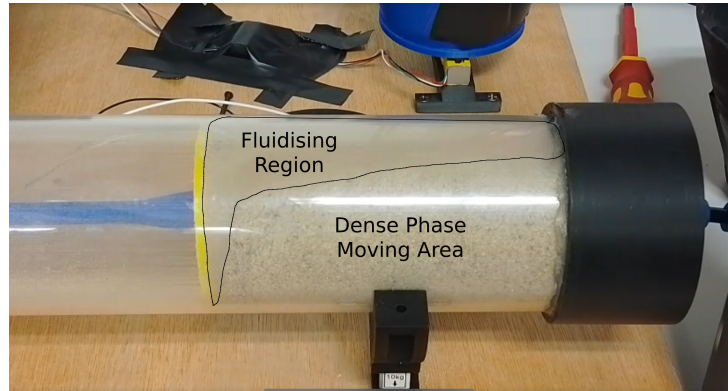


Figure 4.21: A Snapshot of the 2nd 5 bar Inlet Test

whether a fluidising region was also present there, or whether the two regions may have been connected. It is hypothesised that this unexpected fluidisation pattern is due to the particle size of the powder. As discussed in section 2.2, at the micron scale, gravity increasingly influences the fluidisation of larger particles. At the millimetre scale, gravitational effects may dominate entirely.

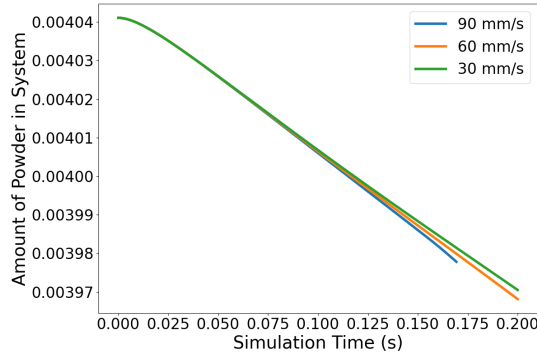
This behaviour was also accompanied by inconsistent piston movement, which progressed in discrete steps rather than with a smooth, continuous velocity. The cause of this behaviour is not well understood, and it is particularly surprising that it is not reflected in any of the mass flow rate data. It is possible that the powder was being rearranged inside the tank in discrete bursts while still being dispensed smoothly, or that redistribution occurred within the pipe as the powder travelled toward the separator. However, further analysis would be required to investigate this effect in detail.

4.6 Numerical Analysis of Mass Flow Rate

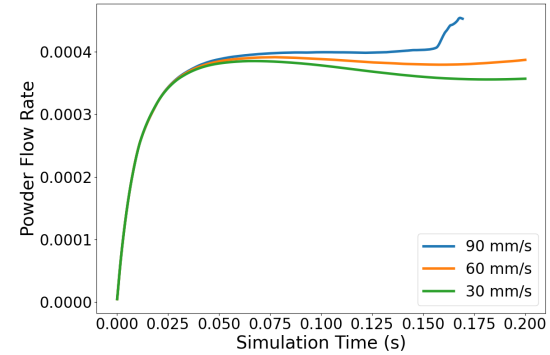
As mentioned in section 3.8, the validity of the simulations, especially given their 2D nature, are unknown. However the numerical investigation did present some potentially useful results.

4.6.1 Results of System Under Microgravity

The investigation into the flow under microgravity was conducted first and the simulation was tuned to this regime. The relationship between mass flow rate and piston velocity was conducted, recording the integration of the particle amount in the system over time as well as recording the particle distributions. As shown in Figure 4.22, the relationship can be somewhat replicated as a positive correlation between mass flow and piston velocity can be seen. Interestingly, the powder mass flow rate initially starts at the same rate and only diverges after



(a) Amount of Powder in the System



(b) Mass Flow Rate of Powder

Figure 4.22: Numerical Results of System Under Microgravity

a time. Even then, it is not consistent, suggesting longer or more detailed simulations could reveal additional information.

The particle distributions at the start, 0.1s in and the end (whether that is 0.2 seconds for the successful simulations or 0.175 for the ones that crashed) are shown in Figure 4.6.1 and Figure 4.6.1.

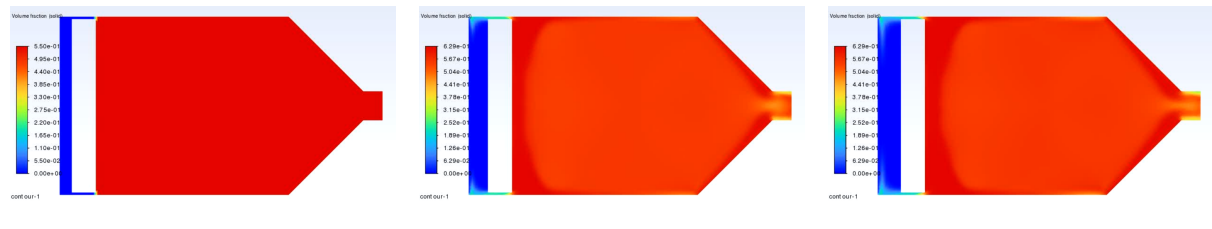


Figure 4.23: Particle Distributions from a Piston Velocity of 30 mm/s



Figure 4.24: Particle Distributions from a Piston Velocity of 90 mm/s

These simulations seem to show two separate regions of particle density. While this could be viewed as supporting the theorised behaviour, outlined in section 3.6, Figure 4.6.1 (c) seems to suggest that when the piston moves fast enough towards the outlet, the fluidised region vanishes. This could be because the piston will move 90 mm/s in the simulation regardless of the force provided by any arching at the tube-cone interface or could be due to physics not captured by the chosen models, either way additional investigations into this could prove fruitful but were not conducted given the time requirements of the project.

4.6.2 Results of System Under Earth's Gravity

The simulations with gravity proved much more problematic. The ethos of the numerical investigation was to set up a system with identical parameters and only change the strength of gravitational force applied. This resulted in the system under gravity being relatively unrepresentative of the experimental phenomena observed. Shown in Figure 4.25, the amount of powder in the system and the corresponding mass flow rate for the 30 mm/s and 90 mm/s piston velocities are shown. Ideally, 60 mm/s would also have been investigated but given the

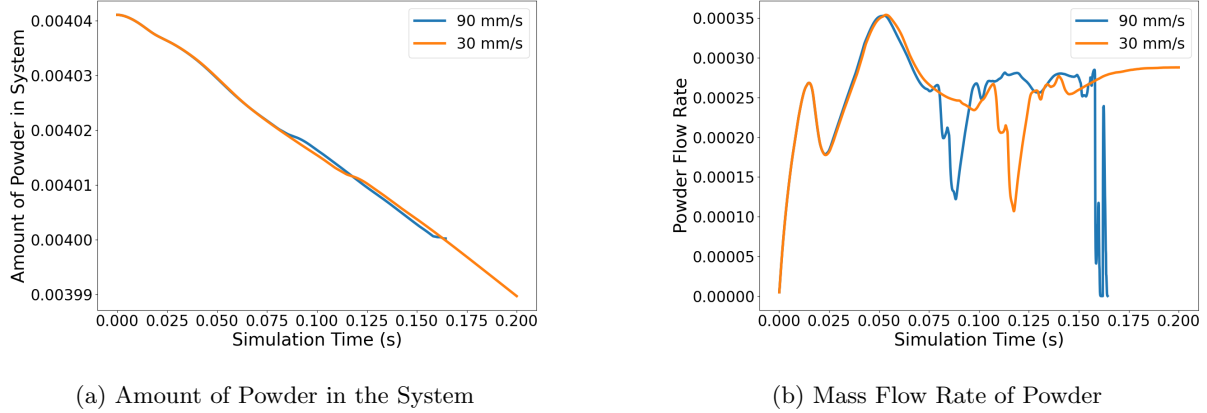


Figure 4.25: Numerical Results of System Under Earth's Gravity

troubleshooting of this behaviour took so long, there was no time to complete this set of studies. This independence of mass flow rate and piston velocity deviates from the literature and experimental results indicate an incorrect formulation of the simulation. The main cause for this is thought to be the value taken for the gravitational constant. Given nothing else to go off of, gravitational acceleration was taken to be 9.81 m/s. Considering the inlet velocity is 0.01 m/s, it is assumed that this was so large that it dominated the behaviour. As seen in Figure 4.6.2 and Figure 4.6.2, the piston still increased compaction at the outlet with the void above the particles being much smaller in the 90 mm/s case. However, there are no visual indications of

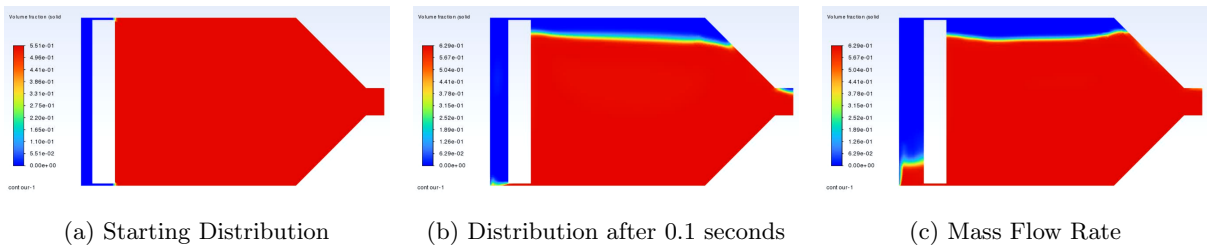


Figure 4.26: Particle Distributions from a Piston Velocity of 30 mm/s

fluidisation and therefore it is assumed that the velocity inlet is too little to promote it. Given more time, a new simulation would be setup, ideally in 3D to ground the inlet parameters and gravity in research-based values.

Also of note, Figure 4.6.2 (c) shows voids near the piston, right before crashing. This is thought to be a symptom of the deformed mesh issue discussed in section 3.8.

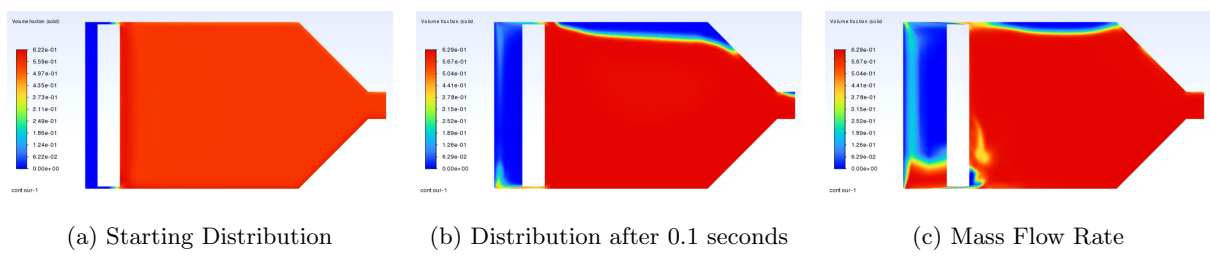


Figure 4.27: Particle Distributions from a Piston Velocity of 90 mm/s

5 Conclusion and Future Work

5.1 Research Objectives and Key Findings

This report set out to investigate and improve the powder feed mechanism for in-space cold spray additive manufacturing, addressing several specific objectives. Additive manufacturing in space has been demonstrated, but only with wire-fed systems, limiting the additive manufacturing techniques available for manufacturing in space.

First, the hypothesised shortcomings of the previous feed system design were analysed and supported by numerical simulations, justifying the need for a subsystem redesigned.

Accordingly, a fluidized powder-bed approach with a pneumatically-driven, gas-permeable piston was chosen as the most promising architecture for feeding powder into a CSAM system. To do this, significant parallels were drawn from previous work on powder feed systems used for metallic powder fed engines and the differences between the two applications were investigated.

From this, a prototype feed-system was designed, manufactured and experimentally evaluated under terrestrial conditions to investigate controllability of mass flow, an important parameter in the cold spray process. The system demonstrated somewhat reliable powder delivery, with mass flow rate responding predictably to changes in input gas pressure. The system achieved powder feed rates on the order of 20 to 60 grams per second, substantially exceeding the throughput of prior comparable systems, which operated only at a few grams per minute. While this may limit comparisons to other work, it expands on the literature available for powder-feed systems designed for additive manufacturing, a current gap in research. The low-pressure, high mass flow rate of this system is rare for powder-feed systems and highlights how much potential the architecture still has to be realised. The results from testing provide strong evidence that the required inlet pressure for effective powder feeding can be significantly reduced, an important finding that could minimises gas consumption and hardware stress in operation.

Another key objective was to optimise the piston geometry and understand its impact on system performance, done through an iterative design process. Early piston prototypes highlighted challenges such as an insufficient pressure force on the piston and jamming due to powder. The insights from these failures informed the final piston design: a lightweight dual-plate piston made of flexible TPU cones connected by a central rod. This compliant geometry provided the necessary resilience against jamming, and the flexibility of the TPU cones, combined with a longer piston span, also helped compensate for manufacturing imperfections allowing the piston to take up the full cross-section of the tank, increasing pressure force on the piston.

Finally, an attempt to analyse performance of the design was conducted through simulations in both microgravity and terrestrial gravity to investigate extrapolation of Earth-based results to space. While time constraints and software limitations hampered the success of this analysis, interesting results for fluidisation in microgravity were still uncovered. A direct comparison

between the two operating conditions was never made.

In conclusion, this report finds no fatal flaws in the use of fluidised powder feed systems for in-space applications but could not quite provide undeniable evidence the system would work as originally desired.

5.2 Suggested Next Steps

Owing to the broad nature of the project, many research aspects were touched upon, but not in great detail. Therefore, future work should begin by refining the fundamental experimental parameters used in system testing to enable a more precise and representative characterisation of the powder and fluidisation dynamics under microgravity conditions.

One immediate improvement involves reducing the size of the powder particles used in the experiments. The current setup, while effective for demonstrating general system functionality, employs relatively large particle sizes that do not fully capture the nuances of granular flow in realistic applications. Finer powders are more representative of those used in additive manufacturing processes and are also more sensitive to gas drag forces, which makes their behaviour under fluidisation and compaction more dependent on subtle variations in system design.

In addition to reducing particle size, future investigations should aim to design a system with a significantly lower mass flow rate. While the high flow rates achieved in the current system demonstrate the scalability of cold spray as a manufacturing process, they also mask smaller-scale fluctuations that could impact part quality or consistency in more delicate applications. Reducing the flow rate would enable a more detailed analysis of the feeder's repeatability and controllability, particularly in the context of long-duration additive manufacturing tasks where material must be dispensed in highly precise, uniform layers.

Alongside these experimental refinements, further computational work is needed to optimise the geometry of the piston itself. While the current design has proven functional, it was developed largely through empirical iteration. Given that the piston strongly influences both fluidisation, by affecting the mass flow rate of gas, and compaction, by affecting the pressure differential through the system. A more rigorous modelling approach—incorporating both fluid-structure interaction and granular material behaviour, could yield significant gains in performance.

Building on this, an important next step is the extension of numerical modelling efforts to evaluate the system's direct applicability to microgravity environments. While current simulations have provided some insight into general flow dynamics, they have not yet fully explored how the absence of gravitational forces affects powder behaviour.

Ultimately, once the system has been refined through these experimental and numerical efforts, full validation under microgravity conditions will be essential. Testing the feeder in drop towers, parabolic flights, or suborbital vehicles would provide invaluable data on its real-world performance and confirm its readiness for integration into in-space manufacturing platforms.

Bibliography

- [1] 911Metallurgist. How to keep bins flowing, n.d. [online] Available at: <https://www.911metallurgist.com/blog/how-to-keep-bins-flowing/> [Accessed 2 June 2025].
- [2] H. Assadi, H. Kreye, F. Gärtner, and T. Klassen. Cold spraying - a materials perspective. *Acta Materialia*, 116:382–407, 2016. Accessed: 2025-05-03.
- [3] Venkata Satish Bhattiprolu, Kyle W. Johnson, Ozan C. Ozdemir, and Grant A. Crawford. Influence of feedstock powder and cold spray processing parameters on microstructure and mechanical properties of ti-6al-4v cold spray depositions. *Surface and Coatings Technology*, 335:1–12, 2018.
- [4] Venkata Sivaram Bitragunta, Todd E. Sparks, and Frank W. Liou. Performance metric for powder feeder systems in additive manufacturing. In *Proceedings of the 26th Annual International Solid Freeform Fabrication Symposium*, pages 473–491, Austin, TX, 2015. University of Texas at Austin.
- [5] Daryl E. Crawmer. Process control and control equipment. In R. C. Jr. Tucker, editor, *Thermal Spray Technology, ASM Handbook, Vol. 5A*, pages 66–75. ASM International, Materials Park, OH, 2013.
- [6] H. Enwald, E. Peirano, and A.-E. Almstedt. Eulerian two-phase flow theory applied to fluidization. *International Journal of Multiphase Flow*, 22(1):21–66, 1996. Accessed: 2025-05-19.
- [7] European Space Agency. Esa launches first metal 3d printer to iss. https://www.esa.int/Science_Exploration/Human_and_Robotic_Exploration/ESA_launches_first_metal_3D_printer_to_ISS, Jan 2024. [Accessed 21 May 2025].
- [8] Jialin Fan, Haitao Yun, Xiaoqiang Zhang, Dongxu Chang, Xin Chu, Yingchun Xie, and Guosheng Huang. High-performance pure aluminum coatings on stainless steels by cold spray. *Coatings*, 13(4), 2023.
- [9] D. Guo, M. Kazasidis, A. Hawkins, N. Fan, Z. Leclerc, D. MacDonald, A. Nastic, R. Nikbakht, R. Ortiz-Fernandez, S. Rahmati, M. Razavipour, P. Richer, S. Yin, R. Lupoi, and B. Jodoin. Cold spray: Over 30 years of development toward a hot future. *Journal of Thermal Spray Technology*, 31(4):866–907, 2022.
- [10] Jason W. Hartwig. A detailed historical review of propellant management devices for low gravity propellant acquisition. Technical report, NASA Glenn Research Center, 2016.
- [11] Mostafa Hassani-Gangaraj, David Veysset, Victor K. Champagne, Keith A. Nelson, and Christopher A. Schuh. Adiabatic shear instability is not necessary for adhesion in cold spray. *Acta Materialia*, 158:430–439, 2018.

- [12] Klaren Technology. Fluidization. <https://klarenbv.com/fluidization/>, 2021. Accessed: 2025-06-11.
- [13] D. Kunii and O. Levenspiel. *Fluidization Engineering*. Robert E. Krieger Publishing Co., Melbourne, FL, 1977.
- [14] Chao Li, Chunbo Hu, Xin Xin, Yue Li, and Haijun Sun. Experimental study on the operation characteristics of aluminum powder fueled ramjet. *Acta Astronautica*, 129:74–81, 2016.
- [15] Chao Li, Xiaofei Zhu, Zhe Deng, Jiangang Yang, Chunbo Hu, and Jinjia Wei. Powder feeding in a powder engine under different gas-solid ratios. *Acta Astronautica*, 189:712–721, 2021.
- [16] Mengzhe Li et al. Application and performance estimation of mg/co₂ engine on mars. Technical Report 2008002287, NASA, 2008. Accessed via NASA Technical Reports Server.
- [17] Adam Malagowski. Additive manufacturing (3d printing) in space: Final year project report. Unpublished undergraduate thesis, Department of Aeronautics, Imperial College London, 2019.
- [18] Yuyi Mao, Juan Hu, Qiang Chen, and Xiaodong Shen. Quantitative analysis of the physical properties of ti6al4v powders used in a powder bed fusion based on 3d x-ray computed tomography images. *Materials*, 17(4), 2024.
- [19] A. Merstallinger, M. Sales, E. Semerad, and B.D. Dunn. Assessment of the cold welding between separable contact due to impact and fretting under vacuum. Technical Report STM-279, European Space Agency, Noordwijk, The Netherlands, 2009.
- [20] My DataBook. Stress for thick-walled cylinders and spheres using lame's equations. <https://www.mydatabook.org/solid-mechanics/stress-for-thick-walled-cylinders-and-spheres-using-lames-equations/>, n.d. Accessed: 14 June 2025.
- [21] NASA. Feasibility of remotely manipulated welding in space - a step in the development of a space manufacturing facility. Technical Report NASA-TM-84678, National Aeronautics and Space Administration (NASA), 1984. Accessed: 2025-05-01.
- [22] Oerlikon Metco. Thermal spray components - feeders (suspension). <https://www.oerlikon.com/metco/en/products-services/thermal-spray-equipment/thermal-spray-components/feeders/?tab=suspension>, 2023. Image accessed November 2023; since removed.
- [23] Ludger Overmeyer, Marvin Raupert, Matthias Pusch, Tjorben Griemsmann, André Katterfeld, and Christoph Lotz. Laser powder directed energy deposition and substrate-free single layer powder bed fusion under micro- and lunar gravity conditions. *CIRP Annals*, 2025.

- [24] T. Prater, N. Werkheiser, F. Ledbetter, D. Timucin, K. Wheeler, and M. Snyder. 3d printing in zero g technology demonstration mission: Complete experimental results and summary of related material modeling efforts. *International Journal of Advanced Manufacturing Technology*, 101(1-4):391–417, Mar 2019.
- [25] Alessandro M. Ralls, Mohammadreza Daroonparvar, Merbin John, Soumya Sikdar, and Pradeep L. Menezes. Solid-state cold spray additive manufacturing of ni-based superalloys: Processing-microstructure-property relationships. *Materials*, 16(7), 2023.
- [26] Red River. Asme factor for pressure vessels. <https://www.redriver.team/asme-factor-for-pressure-vessels/>, 2024. Accessed: 2025-05-29.
- [27] Shabnam Sadeghi Esfahlani. Ballistic performance of polycarbonate and polymethyl methacrylate under normal and inclined dynamic impacts. *Heliyon*, 7(4):e06856, 2021.
- [28] Tao Sheng, Xiaoqiang Fan, Yao Yang, Zhengliang Huang, Jingyuan Sun, Binbo Jiang, Jingdai Wang, Yongrong Yang, and Zuwei Liao. Bubble characterization in the gas-solid fluidized bed using an intrusive acoustic emission sensor array. *Chemical Engineering Journal*, 446:137168, 2022.
- [29] Chad W. Sinclair, Ralf Edinger, Will Sparling, Amin Molavi-Kakhki, and Chantal Labrecque. Vibratory powder feeding for powder bed additive manufacturing using water and gas atomized metal powders. *Materials*, 14(13):3548, 2021.
- [30] Shankar Subramaniam. Lagrangian-eulerian methods for multiphase flows. *Progress in Energy and Combustion Science*, 39(2):215–245, 2013.
- [31] Haijun Sun, Chunbo Hu, Tian Zhang, and Zhe Deng. Experimental investigation on mass flow rate measurements and feeding characteristics of powder at high pressure. *Applied Thermal Engineering*, 102:30–37, 2016.
- [32] Haijun Sun, Chunbo Hu, and Xiaofei Zhu. Numerical simulation on the powder propellant pickup characteristics of feeding system at high pressure. *Acta Astronautica*, 139:85–97, 2017.
- [33] Fatemeh A. Talebi, Zobaideh Haydari, Hamid Salehi, Mozhdeh Mehrabi, Jabbar Gardy, Mike Bradley, Andrew E. Bayly, and Ali Hassanpour. Spreadability of powders for additive manufacturing: A critical review of metrics and characterisation methods. *Particuology*, 93:211–234, 2024.
- [34] Jie Tang, Haifeng Liu, Xiaolei Guo, and Haifeng Liu. Discharge characteristics of non-gravity-driven powder in horizontal silos. *Powder Technology*, 400:117234, 02 2022.
- [35] Jie Tang, Yuxin Yang, Zongtao Wang, Haifeng Lu, and Haifeng Liu. Powder feeding enhancement of powder propellant supply system by using gas-permeable piston. *Powder Technology*, 420:118406, 2023.

- [36] Rodolpho Fernando Vaz, Andrea Garfias, Vicente Albaladejo, Javier Sanchez, and Irene García Cano. A review of advances in cold spray additive manufacturing. *Coatings*, 13(2):267, 2023.
- [37] D. V. Wagle and G. A. Baker. Cold welding: a phenomenon for spontaneous self-healing and shape genesis at the nanoscale. *Materials Horizons*, 2:157–167, 2015.
- [38] U. Zafar, V. Vivacqua, G. Calvert, M. Ghadiri, and J.A.S. Cleaver. A review of bulk powder caking. *Powder Technology*, 313:389–401, 2017.
- [39] Zhicheng Zhang, Zhanqiang Liu, Bing Wang, and Yukui Cai. Effect of plastic deformation of particle and substrate on metallurgical bonding during cold spraying. *Materials Letters*, 373:137157, 2024.
- [40] Ling Zhou, Lingjie Zhang, Ling Bai, Weidong Shi, Wei Li, Chuan Wang, and Ramesh Agarwal. Experimental study and transient cfd/dem simulation in a fluidized bed based on different drag models. *RSC Adv.*, 7:12764–12774, 2017.

A Analysis of Feed Architectures

Configuration	Powder Storage Method	Powder Dispensing Method	Material Resources Required to Operate	Does the Dispensing Mechanism Require Gravity?
Separate Mechanisms	Bladder tank	rotating disk	none	Yes
	Bladder tank	Screw fed	none	No
	Bladder tank	vibration fed	none	Yes
Integrated Storage and Dispensing	Permeable piston tank	Fluidised Powder Bed	gas	No
		liquid suspension feeder	liquid	No

Figure A.1: (a) Start

Where Can Powder Get Stuck?	What are the Power Requirements?	Will there be Issues in Depressurisation?	Will there be Issues in Repressurisation?
valves, disk rotating mechanism rotation of disk and friction against s	pressure leakage through seal bringing particles with it into mechanism	pressure leakage through seal bringing particles with it into nozzle	could cause seal to compress
valves, screw rotating mechanism rotation of screw and friction against pressure leakage through seal bringing particles with it into nozzle			pressure leakage through seal but no particle flow
valves	vibration mechanism	depressurisation will suck particles through mechanism into nozzle	
valves	stronger motors to pump liquid	vapourisation of the liquid, gas bubbles	

Figure A.2: (b) Middle

How Will Mass Flow Rate be Controlled?	Expected Quality of Flow Rate	Prep Time Once Depressurised	Footprint on Rest of Design	Total
speed of rotation	fluctuating due to suction needing to be separated from entire channel	time to do a 180deg rotation		26
speed of screw	medium due to clumping	time taken to move powder from start of screw to end		17
frequency of vibration	medium due to unrefined/novel method	time to start vibrator	vibration could loosen screws	19
pressure differential to control flow rate	high	time to reach p set point		16
valve setpoints or pump strength	high	time to reach p set point		22

Figure A.3: (c) End

Figure A.4: Comparison of Suitability of Design Paradigm Unedited

Configuration	Powder Storage Method	Powder Dispensing Method	Material Resources Required to Operate	Does the Dispensing Mechanism Require Gravity?
Separate Mechanisms	Bladder tank	rotating disk	powder will float up and out of the annular groove or resemble couette flow when being moved from inlet to outlet therefore strong seal between the moving and stationary part of the design as well as reduced transfer rate would be expected and have to be accounted for	
	Bladder tank	Screw fed	No	
	Bladder tank	vibration fed	with nothing forcing the powder from the hopper to the exit chute the design would have to induce gravity through rotation or some other mechanism that would drastically increase the design complexity	
Integrated Storage and Dispensing	Permeable piston tank	Fluidised Powder Bed	gas will need to be there to accelerate the particles anyway so can take from that source but adds additional complexity	No
		liquid suspension feeder	liquid	No

Figure A.5: (a) Start

Where Can Powder Get Stuck?	What are the Power Requirements?	Will there be Issues in Depressurisation?	Will there be Issues in Repressurisation?
a strong mechanical seal would be needed along the entire annular groove	rotating a large disk on a sealed plate surface would require a large force to start initially and then once slipping a continuous force to keep it in motion	as hopper starts at atmospheric pressure as the powder vents the gas it will pass through the seal into the main mechanism dragging powder with it would require a venting line and actuation adding additional complexity	since there will be many packets of powder in a vacuum these may compress upon repressurisation and require strengthening to prevent damage possibly affecting consistency of powder dispensing as well as mass of design
the screw mechanism can be placed far away from the powder so a seal wouldn't need to be as tight and the seal surface would be simple	since seal is weaker the force to overcome it is less	particles will be pulled through the screw with no barrier to stop the pressure from accelerating the particles lots of powder will be lost or an additional venting line will be needed adding additional complexity	pressure could leak back up to the tank which as it will not seal the powder out, it is a complex geometry that means some of the powder will be stopped and valve to connect dispenser can be used to further mitigate powder loss
valves	the mechanism to cause vibrations needs to reach a certain frequency for the entire duration and may need modification to not require vibration even in turned off state	with no barrier to stop the pressure from accelerating the particles lots of powder will be lost or an additional venting line will be needed adding additional complexity	
valves	to reach pressures and speeds required for cold flow a strong electric pump may be needed	this will decrease efficiency of pump or possibly damage impellers so will constrain the types of pumps available for use	

Figure A.6: (b) Middle

How Will Mass Flow Rate be Controlled?	Expected Quality of Flow Rate	Prep Time Once Depressurised	Footprint on Rest of Design	Total
speed of rotation	sticking due to friction could be a large issue requiring either a larger motor or weaker seal. If operating at slow speeds a gearbox could be used but this adds complexity	could size up the motor to allow for a quick movement of powder from storage to dispensing side but will require more power and mass budget		26
speed of screw	different geometries of screw could be used to prevent electrostatic clumping or the interface between screw and gas could be analysed	could size up the motor to allow for a quick movement of powder from storage to dispensing side but will require more power and mass budget		17
$y = 1/x$ is close to the relationship between Hz and mass flow rate meaning not linear but not complex	high	time to start vibrator	vibration resistant screws like locknuts	19
more complex than motor actuation, possibly requiring a control system and testing, could reduce generalisability	high	would need a more advanced controller and faster valves to speed up		16
more complex than motor actuation, possibly requiring a control system and testing, could reduce generalisability	high	would need a more advanced controller and faster valves to speed up		22

Figure A.7: (c) End

Figure A.8: Comparison of Difficulty of Edits Required

B Unprocessed Simulation Images

As the images in section 4.1 are heavily processed, the unprocessed ones are provided here for clarity.

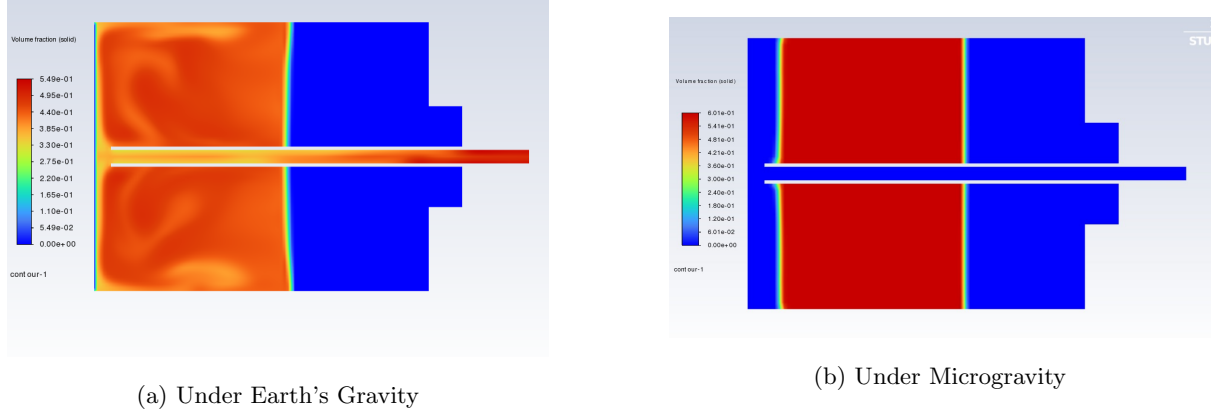


Figure B.1: Phase Density of Old Design after 2 Seconds

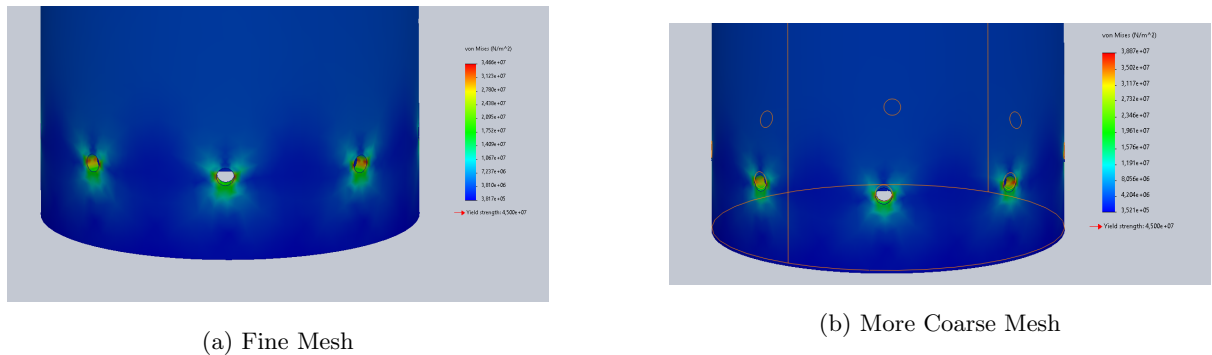


Figure B.2: Results of Tank FEA

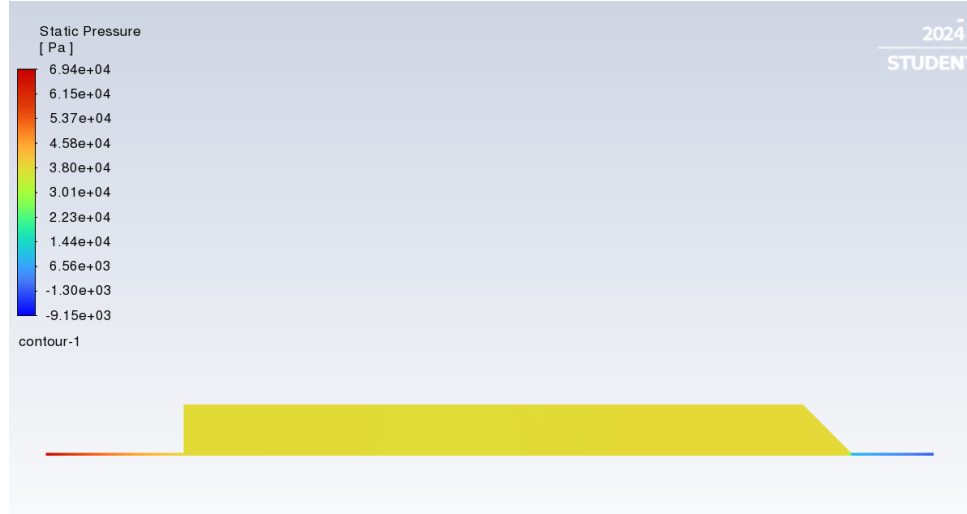


Figure B.3: Static Pressure of Empty Tank Simulation

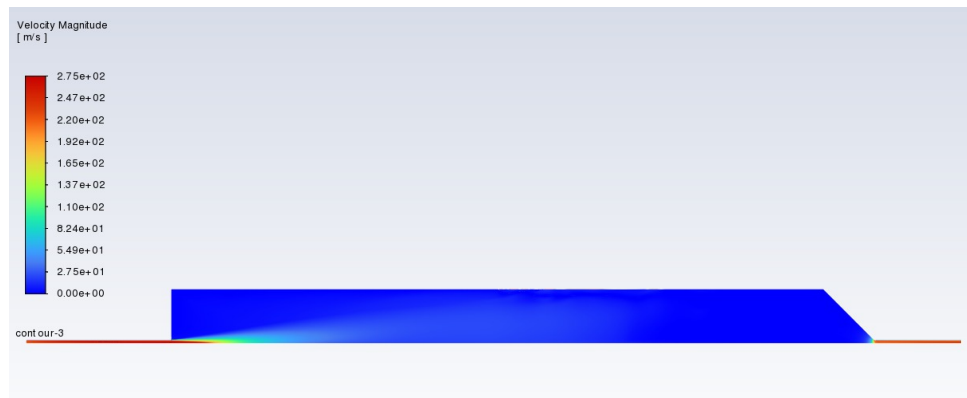


Figure B.4: Velocity Magnitude of Empty Tank Simulation

C End Cap Engineering Drawings

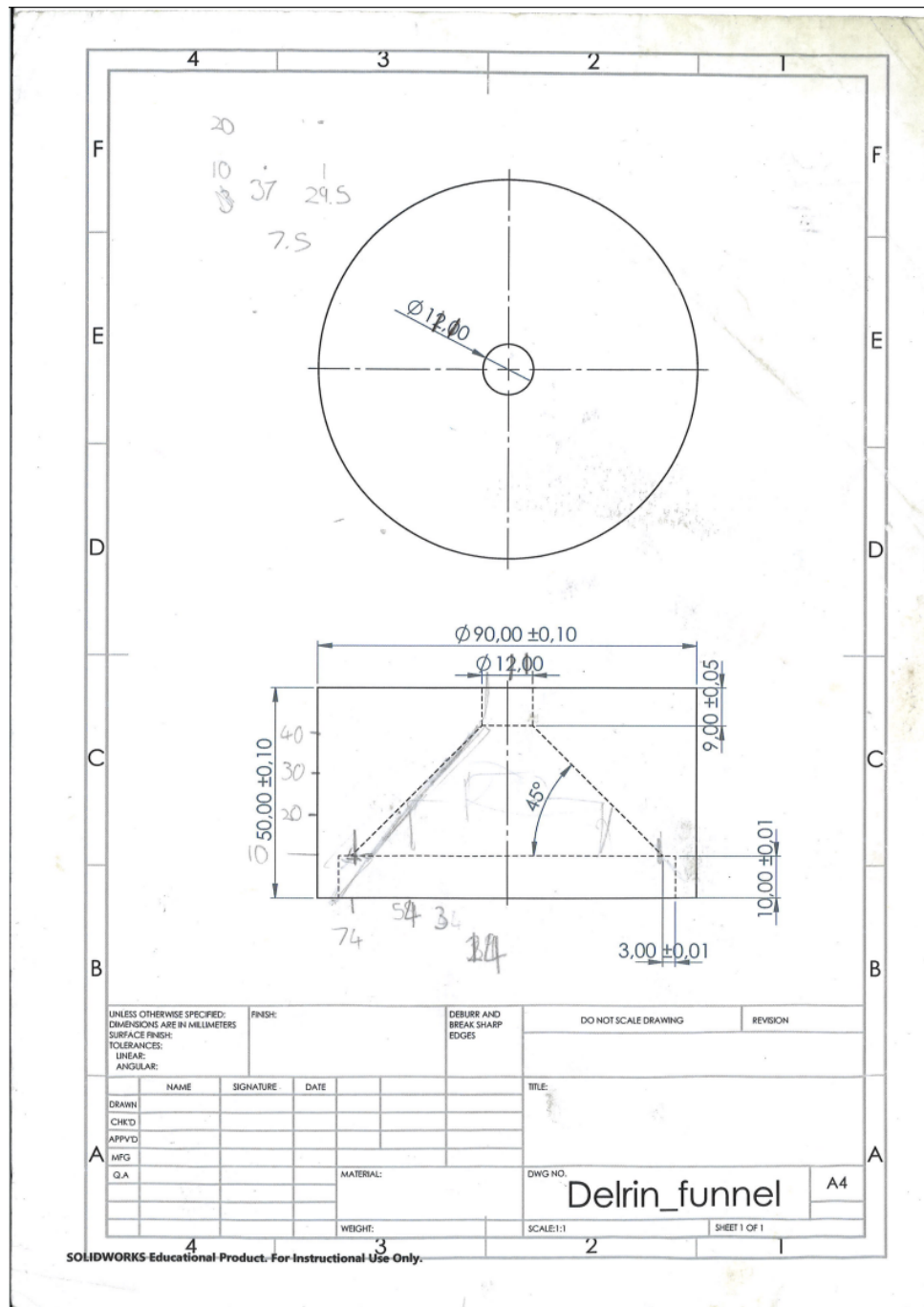


Figure C.1: Outlet End Cap Engineering Drawing

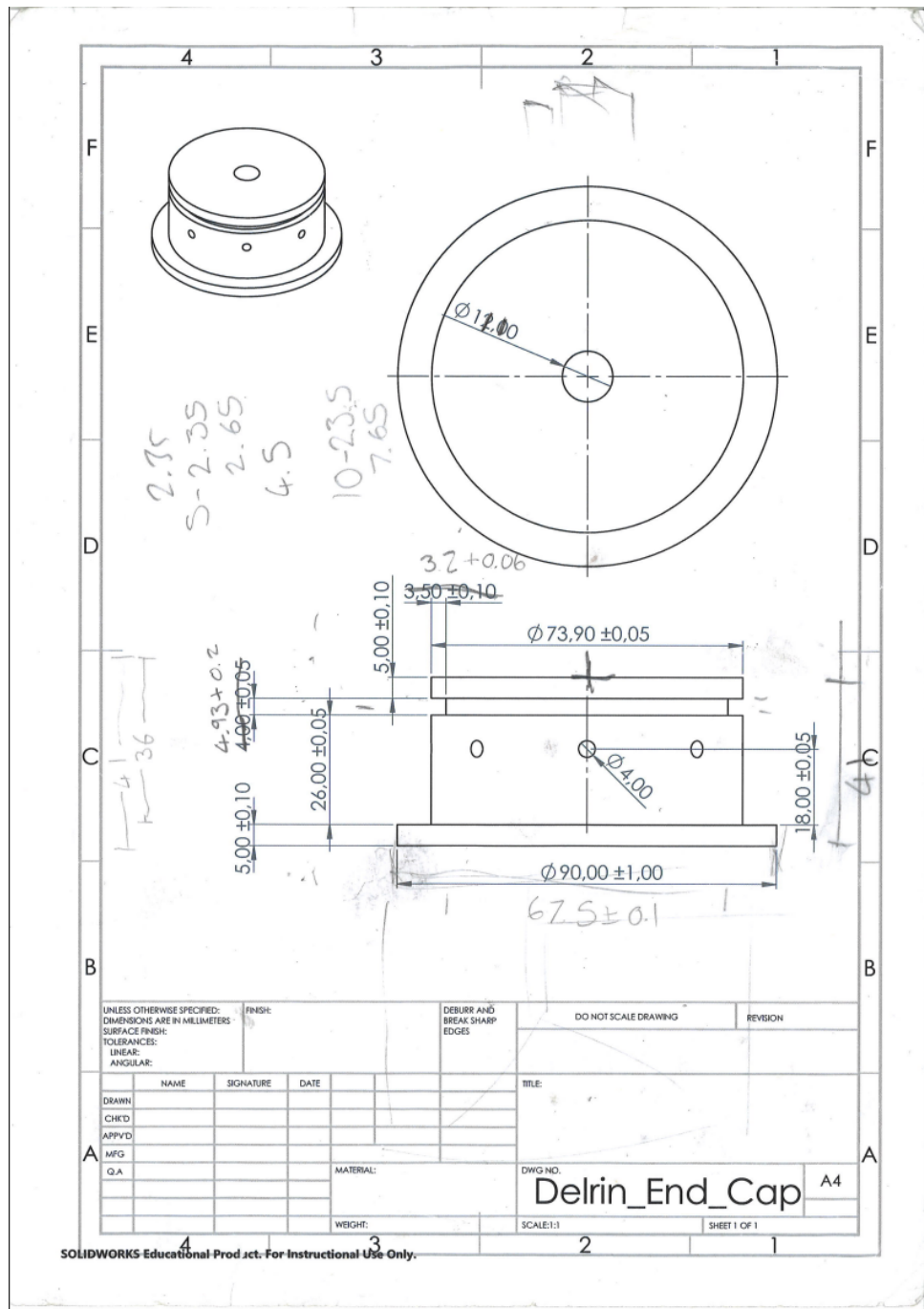


Figure C.2: Inlet End Cap Engineering Drawing

D Mass Flow Analysis Code

Listing D.1: Example Python code for Mass Flow Analysis

```
import matplotlib.pyplot as plt
import pandas as pd

# Read the CSV files
input_file_1 = 'Research_Files/June/5_bar_sand/2_kermit106.csv' # 0 2 7
input_file_2 = 'Research_Files/June/5_bar_sand/2_kermit108.csv' # 0 1 7

# Load the data into a DataFrame
df_1 = pd.read_csv(input_file_1)
df_2 = pd.read_csv(input_file_2)

# Keep only the specified columns
df_1 = df_1[['BackendTime', 'ch0sens', 'ch2sens', 'ch7sens']]
df_2 = df_2[['BackendTime', 'ch0sens', 'ch1sens', 'ch7sens']]

# Rescale BackendTime to seconds and set the first value to 0
df_1['BackendTime'] = (df_1['BackendTime'] - 1748808369580) / 1e3
df_2['BackendTime'] = (df_2['BackendTime'] - 1748808369580) / 1e3

df_1 = df_1[(df_1['BackendTime'] >= 33) & (df_1['BackendTime'] <= 82)]
df_2 = df_2[(df_2['BackendTime'] >= 33) & (df_2['BackendTime'] <= 82)]

plt.rc('legend', fontsize=24)    # Increase legend font size
plt.rc('lines', linewidth=4)    # Further increase line width
plt.rc('axes', labelsize=28)    # Increase axis label font size
plt.figure(figsize=(12, 8))    # Increase figure size
plt.rc('xtick', labelsize=24)    # Increase x-axis tick font size
plt.rc('ytick', labelsize=24)    # Increase y-axis tick font size
# plt.plot(df_1['BackendTime'], df_1['ch0sens'], label='Inlet PT (df_1)') #### use
plt.plot(df_1['BackendTime'], df_1['ch2sens'], label='Start_of_Tank', color='blue')
plt.plot(df_1['BackendTime'], df_1['ch7sens'], label='End_of_Tank', color='red')
plt.plot(df_2['BackendTime'], df_2['ch7sens'], label='Cyclone_Seperator', color='green')
plt.axvline(x=39.5, color='green', linestyle='--')
plt.axvline(x=74.9, color='green', linestyle='--')
# Remove all values before 8 seconds
# Add labels and title
```

```

plt.xlabel('Experiment_Time_(s)')
plt.ylabel('Load_Cell_Values_(kg)')
plt.ylim(0.1, 2.1)
plt.legend()
plt.tight_layout()
# Show the plot
plt.savefig('./latex/report_assets/52_raw_mass.png')
df_1['ch2plus7'] = df_1['ch2sens'] + df_1['ch7sens']
# Save cleaned DataFrames to new CSV files
df_1.to_csv(input_file_1.replace('.csv', '_clean.csv'), index=False)
df_2.to_csv(input_file_2.replace('.csv', '_clean.csv'), index=False)

# import matplotlib.pyplot as plt
# import pandas as pd

# # Read the CSV files
# input_file_1 = 'Research_Files/June/5_bar_sand/2_kermit106_clean.csv'
# 0 2 7
# input_file_2 = 'Research_Files/June/5_bar_sand/2_kermit108_clean.csv'
# 0 1 7

# # Load the data into a DataFrame
# df_1 = pd.read_csv(input_file_1)
# df_2 = pd.read_csv(input_file_2)

# # Keep only the specified columns
# df_1 = df_1[['BackendTime', 'ch0sens', 'ch2sens', 'ch2plus7']]
# df_2 = df_2[['BackendTime', 'ch0sens', 'ch1sens', 'ch7sens']]

# plt.rc('legend', fontsize=24)      # Increase legend font size
# plt.rc('lines', linewidth=4)       # Further increase line width
# plt.rc('axes', labelsize=28)       # Increase axis label font size
# plt.figure(figsize=(12, 8))        # Increase figure size
# plt.rc('xtick', labelsize=24)       # Increase x-axis tick font size
# plt.rc('ytick', labelsize=24)       # Increase y-axis tick font size

# plt.plot(df_1['BackendTime'], df_1['ch2plus7'], label='Combined Tank', color='red')
# plt.plot(df_2['BackendTime'], df_2['ch7sens'], label='Cyclone Seperator', color='blue')

# plt.axvline(x=39.5, color='green', linestyle='--')

```

```

# plt.axvline(x=74.9, color='green', linestyle='--')
## Add labels and title
# plt.xlabel('Experiment Time (s)')
# plt.ylabel('Load Cell Values (kg)')
# plt.legend()
# plt.tight_layout()
## plt.show()
## Show the plot
# plt.savefig('./latex/report_assets/52_clean_mass.png')

# import matplotlib.pyplot as plt
# import pandas as pd

## Read the CSV files
# input_file_1 = 'Research_Files/June/5_bar_sand/2_kermit106_clean.csv'
# 0 2 7
# input_file_2 = 'Research_Files/June/5_bar_sand/2_kermit108_clean.csv'
# 0 1 7

## Load the data into a DataFrame
# df_1 = pd.read_csv(input_file_1)
# df_2 = pd.read_csv(input_file_2)

# df_1 = df_1[['BackendTime', 'ch0sens', 'ch2sens', 'ch2plus7']]
# df_2 = df_2[['BackendTime', 'ch0sens', 'ch1sens', 'ch7sens']]

# df_1['ch2plus7'] = -1*df_1['ch2plus7']
# df_1['m_flow'] = df_1['ch2plus7'].diff()
# df_2['m_flow'] = df_2['ch7sens'].diff()

## Apply a rolling mean to smooth the curves
# window_size = 100 # Adjust as needed for smoothing
# df_1['smooth_combined'] = df_1['ch2plus7'].rolling(window=window_size, center=True).mean()
# df_2['smooth_ch7sens'] = df_2['ch7sens'].rolling(window=window_size, center=True).mean()

# df_1['m_flow_smooth'] = df_1['smooth_combined'].diff()*10
# df_2['m_flow_smooth'] = df_2['smooth_ch7sens'].diff()*10

# plt.rc('legend', fontsize=24)    # Increase legend font size
# plt.rc('lines', linewidth=4)     # Further increase line width
# plt.rc('axes', labelsize=28)     # Increase axis label font size
# plt.figure(figsize=(12, 8))      # Increase figure size

```

```

# plt.rc('xtick', labelsize=24)      # Increase x-axis tick font size
# plt.rc('ytick', labelsize=24)      # Increase y-axis tick font size

# plt.plot(df_1['BackendTime'], df_1['m_flow_smooth']*1000, label='Combined Tank')
# plt.plot(df_2['BackendTime'], df_2['m_flow_smooth']*1000, label='Cyclone Sepera')

# plt.axvline(x=39.5, color='green', linestyle='--')
# plt.axvline(x=49.5, color='red', linestyle='--')
# plt.axvline(x=59.9, color='red', linestyle='--')
# plt.axvline(x=74.9, color='green', linestyle='--')

# plt.xlabel('Experiment Time (s)')
# plt.ylabel('Mass Flow Rate (g/s)')
# plt.ylim(-10, 52)
# plt.legend(loc='lower center')
# plt.tight_layout()
## ## Show the plot
# plt.savefig('./latex/report_assets/52_clean_flow_100.png')

```

As you can most-likely tell, some of this code was written with the help of ChatGPT.